Mixed-Valent {Fe^{IV}(μ-O)(μ-carboxylato)$_2$Fe^{III}}$^{3+}$ Core

Leonardo D. Slep,[†] Ana Mijovilovich,[‡] Wolfram Meyer-Klaucke,[‡]
Thomas Weyhermüller,[†] Eckhard Bill,[†] Eberhard Bothe,[†] Frank Neese,[†] and
Karl Wieghardt*,[†]

*Contribution from the Max-Planck-Institut für Bioanorganische Chemie, Stiftsstrasse 34-36,
D-45470 Mülheim an der Ruhr, Germany and DESY, EMBL, Notkestrasse 85, Geb. 25A,
D-22607 Hamburg, Germany*

Received June 24, 2003; E-mail: wieghardt@mpi-muelheim.mpg.de

Abstract: The symmetrically ligated complexes **1**, **2**, and **3** with a (μ-oxo)bis(μ-acetato)diferric core can be one-electron oxidized electrochemically or chemically with aminyl radical cations [•NR$_3$][SbCl$_6$] in acetonitrile yielding complexes which contain the mixed-valent {(μ-oxo)bis(μ-acetato)iron(IV)iron(III)}$^{3+}$ core: [([9]aneN$_3$)$_2$Fe^{III}$_2$(μ-O)(μ-CH$_3$CO$_2$)$_2$](ClO$_4$)$_2$ (**1**(ClO$_4$)$_2$), [(Me$_3$[9]aneN$_3$)$_2$Fe^{III}$_2$(μ-O)(μ-CH$_3$CO$_2$)$_2$](PF$_6$)$_2$ (**2**(PF$_6$)$_2$), and [(tpb)$_2$Fe^{III}$_2$(μ-O)(μ-CH$_3$CO$_2$)$_2$] (**3**) where ([9]aneN$_3$) is the neutral triamine 1,4,7-triazacyclononane and (Me$_3$[9]aneN$_3$) is its tris-*N*-methylated derivative, and (tpb)$^-$ is the monoanion trispyrazolylborate. The asymmetrically ligated complex [(Me$_3$[9]aneN$_3$)Fe^{III}$_2$(μ-O)(μ-CH$_3$CO$_2$)$_2$Fe^{III}(tpb)](PF$_6$) (**4**(PF$_6$)) and its one-electron oxidized form [**4**^{ox}]$^{2+}$ have also been prepared. Finally, the known heterodinuclear species [(Me$_3$[9]aneN$_3$)Cr^{III}(μ-O)(μ-CH$_3$CO$_2$)$_2$Fe([9]aneN$_3$)](PF$_6$)$_2$ (**5**(PF$_6$)$_2$) can also be one-electron oxidized yielding [**5**^{ox}]$^{3+}$ containing an iron(IV) ion. The structure of **4**(PF$_6$)·0.5CH$_3$CN·0.25(C$_2$H$_5$)$_2$O has been determined by X-ray crystallography and that of [**5**^{ox}]$^{2+}$ by Fe K-edge EXAFS-spectroscopy (Fe^{IV}−O$_{oxo}$: 1.69(1) Å; Fe^{IV}−O$_{carboxylato}$ 1.93(3) Å, Fe^{IV}−N 2.00(2) Å) contrasting the data for **5** (Fe^{III}−O$_{oxo}$ 1.80 Å; Fe^{III}−O$_{carboxylato}$ 2.05 Å, Fe−N 2.20 Å). [**5**^{ox}]$^{2+}$ has an S$_t$ = ^{1}/$_2$ ground state whereas all complexes containing the mixed-valent {Fe^{IV}(μ-O)(μ-CH$_3$CO$_2$)$_2$Fe^{III}}$^{3+}$ core have an S$_t$ = ^{3}/$_2$ ground state. Mössbauer spectra of the oxidized forms of complexes clearly show the presence of low spin Fe^{IV} ions (isomer shift ∼0.02 mm s^{-1}, quadrupole splitting ∼1.4 mm s^{-1} at 80 K), whereas the high spin Fe^{III} ion exhibits δ ≈ 0.46 mm s^{-1} and ΔE_Q ≈ 0.5 mm s^{-1}. Mössbauer, EPR spectral and structural parameters have been calculated by density functional theoretical methods at the BP86 and B3LYP levels. The exchange coupling constant, J, for diiron complexes with the mixed-valent Fe^{IV}−Fe^{III} core (H = −2J S$_1$·S$_2$; S$_1$ = ^{5}/$_2$; S$_2$ = 1) has been calculated to be −88 cm^{-1} (intramolecular antiferromagnetic coupling) and for the reduced diferric form of −75 cm^{-1} in reasonable agreement with experiment (J = −120 cm^{-1}).

Introduction

In 1983, exactly 20 years ago, two groups independently published the synthesis and characterization of two complexes containing the (μ-oxo)bis(μ-carboxylato)diiron(III) core.[1,2] Armstrong and Lippard[1] made use of the tridentate ligand tris-(pyrazolylborate), (tpb)[1−], whereas our group[2] used 1,4,7-triazacyclononane, ([9]aneN$_3$), and its *N*-methylated derivative, (Me$_3$[9]aneN$_3$).[3] The complexes [(tpb)$_2$Fe^{III}$_2$(μ-O)(μ-CH$_3$CO$_2$)$_2$] (**3**),[1] [([9]aneN$_3$)$_2$Fe^{III}$_2$(μ-O)(μ-CH$_3$CO$_2$)$_2$](ClO$_4$)$_2$ (**1**(ClO$_4$)$_2$),[2] and [(Me$_3$[9]aneN$_3$)$_2$Fe^{III}$_2$(μ-O)(μ-CH$_3$CO$_2$)$_2$](PF$_6$)$_2$ (**2**(PF$_6$)$_2$)[3,4] have been described as archetypical models for the differic active

sites of some non-heme metalloproteins such as metazido-hemerythrin,[5] ribonucleotide reductase,[6] and methane monoxygenase[7] (Scheme 1).

Quite early on, it was shown[4] that reversible or quasireversible one electron reduction of the model complex **2** generates a mixed-valent Fe^{II}Fe^{III} (S$_t$ = ^{1}/$_2$) form in CH$_2$Cl$_2$ solution.

Despite the fact that it is safely established that in the catalytic cycles of ribonucleotide reductase and methane monoxygenase high valent iron(IV) ions are involved[10] as compounds X[8] and Q,[9] respectively, it has not been possible to assemble low molecular weight model complexes containing either the mixed-
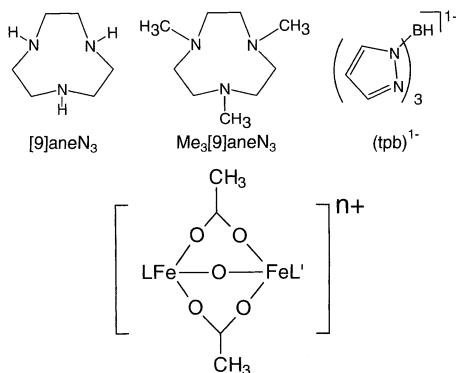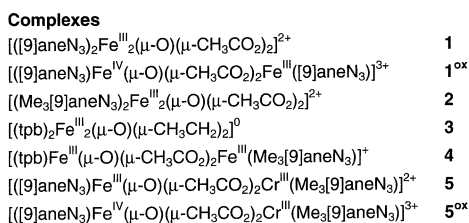
[†] Max-Planck-Institut für Bioanorganische Chemie.
[‡] DESY, EMBL Hamburg.

(1) (a) Armstrong, W. H.; Lippard, S. J. *J. Am. Chem. Soc.* **1983**, *105*, 4837. (b) Armstrong, W. H.; Spool, A.; Papaefthymiou, G. C.; Frankel, R. B.; Lippard, S. J. *J. Am. Chem. Soc.* **1984**, *106*, 3653.
(2) (a) Wieghardt, K.; Pohl, K.; Gebert, W. *Angew. Chem., Int. Ed. Engl.* **1983**, *22*, 727. (b) Spool, A.; Williams, I. D.; Lippard, S. J. *Inorg. Chem.* **1985**, *24*, 2156.
(3) Chaudhuri, P.; Wieghardt, K.; Nuber, B.; Weiss, J. *Angew. Chem., Int. Ed. Engl.* **1985**, *24*, 778.
(4) Hartman, J. R.; Rardin, R. L.; Chaudhuri, P.; Pohl, K.; Wieghardt, K.; Nuber, B.; Weiss, J.; Papaefthymiou, G. C.; Frankel, R. B.; Lippard, S. J. *J. Am. Chem. Soc.* **1987**, *109*, 7387.

(5) (a) Wilkins, R. G.; Harrington, P. C. *Adv. Inorg. Biochem.* **1983**, *5*, 51. (b) Wilkins, P. C.; Wilkins, R. G. *Coord. Chem. Rev.* **1987**, *79*, 195.
(6) (a) Sjöberg, B.-M.; Gräslund, A. *Adv. Inorg. Biochem.* **1983**, *5*, 87. (b) Lammers, M.; Follmann, H. *Struct. Bonding* **1983**, *54*, 27.
(7) (a) Woodland, M. P.; Patil, D. S.; Cammack, R.; Dalton, H. *Biochim. Biophys. Acta* **1986**, *873*, 237. (b) Wallar, B. J.; Lipscomb, J. D. *Chem. Rev.* **1996**, *96*, 2625.
(8) (a) Sturgeon, B. E.; Burdi, D.; Chen, S.; Huynh, B. H.; Edmondson, D. E.; Stubbe, J.; Hoffman, B. M. *J. Am. Chem. Soc.* **1996**, *118*, 7551. (b) Riggs-Gelasco, P.; Shu, L.; Chen, S.; Burdi, D.; Huynh, B. H.; Que, L., Jr.; Stubbe, J. *J. Am. Chem. Soc.* **1998**, *120*, 849. (c) Willems, J.-P.; Lee, H.-I.; Burdi, D.; Doan, P. E.; Stubbe, J.; Hoffman, B. M. *J. Am. Chem. Soc.* **1997**, *119*, 9816.

Scheme 1

Complexes

[(([9]aneN$_3$)$_2$Fe^{III}$_2$(μ-O)(μ-CH$_3$CO$_2$)$_2$]$^{2+}$ **1**

[(([9]aneN$_3$)$_2$Fe^{IV}(μ-O)(μ-CH$_3$CO$_2$)$_2$Fe^{III}([9]aneN$_3$)]$^{3+}$ **1^{ox}**

[(Me$_3$[9]aneN$_3$)$_2$Fe^{III}$_2$(μ-O)(μ-CH$_3$CO$_2$)$_2$]$^{2+}$ **2**

[(tpb)$_2$Fe^{III}$_2$(μ-O)(μ-CH$_3$CH$_2$)$_2$]^{0} **3**

[(tpb)Fe^{III}(μ-O)(μ-CH$_3$CO$_2$)Fe^{III}(Me$_3$[9]aneN$_3$)]$^{+}$ **4**

[(([9]aneN$_3$)Fe^{III}(μ-O)(μ-CH$_3$CO$_2$)$_2$Cr^{III}(Me$_3$[9]aneN$_3$)]$^{2+}$ **5**

[(([9]aneN$_3$)Fe^{IV}(μ-O)(μ-CH$_3$CO$_2$)$_2$Cr^{III}(Me$_3$[9]aneN$_3$)]$^{3+}$ **5^{ox}**

valent {Fe^{III}Fe^{IV}(μ-O)(μ-carboxylato)$_2$}$^{3+}$ core or its homovalent analogue with an {Fe^{IV}$_2$(μ-O)(μ-carboxylato)$_2$}$^{4+}$ unit. It has recently been possible to generate the Fe^{III}Fe^{IV} form of methane monooxygenase via γ-radiolysis.[9d]

A few mixed-valent Fe^{III}Fe^{IV} species containing a diamond core {Fe^{III}(μ-O)$_2$Fe^{IV}}$^{3+}$ have been described.[10–12] Even a dinuclear species with a {Fe^{IV}(μ-O)$_2$Fe^{IV}}$^{4+}$ core[13] has been recently reported. These compounds have been generated as models for the intermediates X in ribonucleotide reductase and Q in methane monooxygenase. The relatively short Fe···Fe distances at $\sim$2.5 Å in these high valent diiron metalloprotein intermediates and the synthetic diamond core model complexes agree nicely. The reactivity of these model complexes toward C–H activation has been studied.

We have now discovered that the symmetric model complexes **1**, **2**, and **3** containing the (μ-oxo)bis(μ-carboxylato)diferric core (Scheme 1) can be one-electron oxidized in dry acetonitrile electrochemically, or chemically by using aminyl radical cations, [$\dot{N}$R$_3$]$^{+}$. Surprisingly, the respective complexes containing the (μ-oxo)bis(μ-acetato)iron(IV)iron(III) mixed valence core are quite stable in solution at temperatures < –20 °C in the absence of a reducing agent. Therefore, it has been possible to record

their UV–vis, EPR, and Mössbauer spectra. X-ray absorption near edge spectra (XANES) and EXAFS spectra have also been measured, which allows the electronic and structural characterization of this new mixed-valent core.

We have also synthesized and characterized the *asymmetric* species [(Me$_3$[9]aneN$_3$)Fe^{III}(μ-O)(μ-CH$_3$CO$_2$)$_2$Fe^{III}(tpb)](PF$_6$) (**4**(PF$_6$)) and its one-electron oxidized form [**4^{ox}**]$^{2+}$.

Finally, we have discovered that one-electron oxidation of the heterodinuclear dication [(Me$_3$[9]aneN$_3$)Cr^{III}(μ-O)(μ-CH$_3$-CO$_2$)$_2$Fe^{III}([9]aneN$_3$)]$^{2+}$ in **5**(PF$_6$)$_2$[14,15] yields the trication [(([9]-aneN$_3$)Fe^{IV}(μ-O)(μ-CH$_3$CO$_2$)$_2$Cr^{III}(Me$_3$[9]aneN$_3$)]$^{3+}$ (**5^{ox}**), where the single ferric ion has been oxidized to an Fe(IV) ion with retention of the overall atom connectivities in the dinuclear species.

Experimental Section

The following complexes have been prepared as described in the literature: [(([9]aneN$_3$)FeCl$_3$],[4] [(Me$_3$[9]aneN$_3$)FeCl$_3$],[4] [(Me$_3$[9]aneN$_3$)-CrBr$_3$],[16] [(tpb)FeCl$_3$] (NEt$_4$),[17] **1**(PF$_6$)$_2$,[2] **2**(PF$_6$)$_2$,[3,4] **3**,[17] and **5**(PF$_6$)$_2$.[14] ^{57}Fe labeled (> 80%) materials were obtained by using ^{57}FeCl$_3$ [18] as starting material. The neutral species **3** has been prepared following Armstrong and Lippard's published procedure[1] or, alternatively, by hydrolysis of [(tpb)FeCl$_3$](NEt$_4$) with sodium acetate.[17] This procedure provided a simple route to ^{57}Fe-enriched samples of **3** (and **5**) by using [^{57}Fe(tpb)Cl$_3$](NEt$_4$) as starting material.

[(tpb)Fe^{III}(μ-O)(μ-CH$_3$CO$_2$)Fe^{III}(Me$_3$[9]aneN$_3$)]PF$_6$ (4(PF$_6$)). A solution of [(tpb)FeCl$_3$](NEt$_4$) (93 mg; 0.184 mmol), [(Me$_3$[9]aneN$_3$)-FeCl$_3$] (61 mg; 0.183 mmol), anhydrous sodium acetate (170 mg; 2.1 mmol) in 25 mL of ethanol (not previously dried) was stirred at room temperature for 24 h. To the filtered solution was then added [NH$_4$]-PF$_6$ (46 mg; 0.28 mmol). After standing of the solution at –18 °C for 24 h a red brown solid material had precipitated which was collected by filtration, washed with ethanol (5 mL) and air-dried. Yield: 117 mg (82%). Single crystals of **4**(PF$_6$)·0.5CH$_3$CN·0.25(C$_2$H$_5$)$_2$O suitable for X-ray crystallography were grown from an acetonitrile solution (4 mL) of the above crude product by slow diffusion of diethyl ether at 20 °C. Red needles (66 mg) were obtained. Anal. Calcd for C$_{24}$H$_{41}$-BN$_{9.5}$O$_{5.25}$F$_6$PFe$_2$: C, 35.41; H, 5.08; N, 16.34; Fe, 13.72. Found: C, 35.4; H, 5.1; N, 16.5; Fe, 13.4. Electrospray mass spectrometry (CH$_3$-CN): *m/z* = 630.3 {**4**}$^{+}$.

[(([9]aneN$_3$)Fe^{IV}(μ-O)(μ-CH$_3$CO$_2$)$_2$Fe^{III}([9]aneN$_3$)](PF$_6$)$_{1.5}$(SbCl$_6$)$_{1.5}$· CH$_2$Cl$_2$([1^{ox}](PF$_6$)$_{1.5}$(SbCl$_6$)$_{1.5}$·CH$_2$Cl$_2$). Under an Ar blanketing atmosphere, a solution of **1**(PF$_6$)$_2$ (51 mg; 0.064 mmol) in dry CH$_2$Cl$_2$ (12 mL) was treated at –30 °C with a solution of [NR$_3$](SbCl$_6$) (R = 2,4-dibromophenyl)[19] (70 mg; 0.066 mmol) in cold dry CH$_2$Cl$_2$ (4 mL). After the addition was completed, within 5 min, a deep red microcrystalline precipitate formed, which was collected by filtration, washed with cold CH$_2$Cl$_2$, and dried in vacuo while keeping the temperature at –40 °C. Anal. Calcd for C$_{17}$H$_{38}$N$_6$O$_5$F$_9$P$_{1.5}$Cl$_{11}$Fe$_2$Sb$_{1.5}$: C, 15.61; H, 2.93; N, 6.42; Fe, 8.54. Found: C, 15.6; H, 2.9; N, 6.4; Fe, 8.5. Electrospray mass spectra (CH$_3$CN): pos. ion: *m/z* = 168.0 {**1^{ox}**}$^{3+}$; neg. ion: *m/z* = 145.0 (PF$_6$)$^{-}$; 331 (SbCl$_6$)$^{-}$.

[(([9]aneN$_3$)Fe^{IV}(μ-O)(μ-CH$_3$CO$_2$)$_2$Cr^{III}(Me$_3$[9]aneN$_3$)](PF$_6$)$_2$(SbCl$_6$)· 2CH$_2$Cl$_2$·2CH$_3$CN (5^{ox}(PF$_6$)$_2$(SbCl$_6$)·2CH$_2$Cl$_2$·2CH$_3$CN). To a sus-

(9) (a) Lee, S.-K.; Nesheim, J. C.; Lipscomb, J. D. *J. Biol. Chem.* **1993**, *268*, 21569. (b) Lee, S.-K.; Fox, B. G.; Froland, W. A.; Lipscomb, J.; Münck, E. *J. Am. Chem. Soc.* **1993**, *115*, 6450. (c) Liu, K. E.; Valentine, A. M.; Wang, D.; Huynh, B. H.; Edmondson, D. E.; Salifoglou, A.; Lippard, S. J. *J. Am. Chem. Soc.* **1995**, *117*, 10 174. (d) Valentine, A. M.; Tavares, P.; Pereira, A. S.; Davydov, R.; Krebs, C.; Hoffman, B. M.; Edmondson, D. E.; Huynh, B. H.; Lippard, S. J. *J. Am. Chem. Soc.* **1998**, *120*, 2190.

(10) Que, L.; Jr. *Pure Appl. Chem.* **1998**, *70*, 947. (b) Que, L., Jr.; Dong, Y. *Acc. Chem. Res.* **1996**, *29*, 190.

(11) (a) Dong, Y.; Fujii, H.; Hendrich, M. P.; Leising, R. A.; Pan, G.; Randall, C. R.; Wilkinson, E. C.; Zang, Y.; Que, L., Jr.; Fox, B. G.; Kauffmann, K.; Münck, E. *J. Am. Chem. Soc.* **1995**, *117*, 2778. (b) Dong, Y.; Que, L., Jr.; Kauffmann, K.; Münck, E. *J. Am. Chem. Soc.* **1995**, *117*, 11 377. (c) Dong, Y.; Zang, Y.; Shu, L.; Wilkinson, E. C.; Kauffmann, K.; Münck, E.; Que, L., Jr. *J. Am. Chem. Soc.* **1997**, *119*, 12 683. (d) Kim, C.; Dong, Y.; Que, L., Jr. *J. Am. Chem. Soc.* **1997**, *119*, 3635.

(12) (a) Zang, Y.; Dong, Y.; Que, L., Jr.; Kauffmann, K.; Münck, E. *J. Am. Chem. Soc.* **1995**, *117*, 1169. (b) Zheng, H.; Zang, Y.; Dong, Y.; Young, V. G., Jr.; Que, L., Jr. *J. Am. Chem. Soc.* **1999**, *121*, 2226. (c) Hsu, H.-F.; Dong, Y.; Shu, L.; Young, V. G.; Que, L., Jr. *J. Am. Chem. Soc.* **1999**, *121*, 5230. (d) Lee, D.; Du Bois, J.; Petrasis, D.; Hendrich, M. P.; Krebs, C.; Huynh, B. H.; Lippard, S. J. *J. Am. Chem. Soc.* **1999**, *121*, 9893.

(13) Costas, M.; Rohde, J.-U.; Stubna, A.; Ho, R. Y. N.; Quaroni, L.; Münck, E.; Que, L., Jr. *J. Am. Chem. Soc.* **2001**, *123*, 12 931.

(14) Hotzelmann, R.; Wieghardt, K.; Flörke, U.; Haupt, H.-J.; Weatherburn, D. C.; Bonvoisin, J.; Blondin, G.; Girerd, J.-J. *J. Am. Chem. Soc.* **1992**, *114*, 1681.

(15) Rodriguez, J. H.; Xia, Y.-M.; Debrunner, P. G.; Chaudhuri, P.; Wieghardt, K. *J. Am. Chem. Soc.* **1996**, *118*, 7542.

(16) Chaudhuri, P.; Winter, M.; Küppers, H.-J.; Wieghardt, K.; Nuber, B.; Weiss, J. *Inorg. Chem.* **1987**, *26*, 3302.

(17) Cho, S. H.; Whang, D.; Han, K. N.; Kim, K. *Inorg. Chem.* **1992**, *31*, 519.

(18) Grapperhaus, C. A.; Mienert, B.; Bill, E.; Weyhermüller, T.; Wieghardt, K. *Inorg. Chem.* **2000**, *39*, 5306.

(19) (a) Schmidt, W.; Steckhan, E. *Chem. Ber. – Recl.* **1980**, *113*, 577. (b) Conelly, N. G.; Geiger, W. E. *Chem. Rev.* **1996**, *96*, 877. (c) Baker, T. N.; Doherty, W. P.; Kelley, W. S.; Newmeyer, W.; Rogers, J. E.; Spalding, R. E.; Walker, R. I. *J. Org. Chem.* **1965**, *30*, 3714.

pension of **5**$(PF_6)_2$ (50 mg; 0.060 mmol) in dry CH_2Cl_2 (7 mL) under an argon blanketing atmosphere was added dropwise 2.5 mL of dry acetonitrile at -30 °C yielding a clear blue solution. A solution of 66 mg (0.063 mmol) of $[NR_3](SbCl_6)$ (R = 2,4-dibromophenyl)[19] in 9 mL of CH_2Cl_2 at -30 °C was added dropwise through a Teflon needle over a period of 15 min to the above solution of **5**$(PF_6)_2$. Another 4 mL of cold CH_2Cl_2 were then added initiating the precipitation of *pale violet* microcrystals which were collected by filtration and washed with cold CH_2Cl_2 and dried in vacuo at low temperature (~ -15 °C). Anal. Calcd for $C_{25}H_{52}N_8O_5F_{12}P_2Cl_{10}CrFeSb$: C, 21.16; H, 3.69; N, 7.90; Fe, 3.94; Cr, 3.66. Found: C, 21.1; H, 3.7; N, 7.7; Fe, 3.6; Cr, 3.9. Electrospray mass spectrum (CH_3CN): $m/z = 180.8$ {**5**^{ox}}$^{3+}$, 271.1 {**5**}$^{2+}$, 561.3 {**5**F}$^+$.

Physical Methods. Infrared spectra as KBr pellets were measured on a Perkin-Elmer 2000 FT-IR/FT-NIR spectrometer with a resolution of 4 cm^{-1}. Elemental analysis were performed by H. Kolbe Mikroanalysis in Mülheim an der Ruhr. Electrospray ionization mass spectra were recorded using a Finnigan MAT 95 spectrometer, Finnigan GmbH, Bremen, Germany. Cyclic voltammetry (CV) was performed under argon with an EG&G potentiostat/galvanostat (model 273A) in dry acetonitrile with 0.1 M tetra-*n*-butylammoniumhexafluorophosphate ($TBAPF_6$) as supporting electrolyte on a standard three electrode cell (glassy carbon working electrode, a platinum net as the counterelectrode and $Ag/AgNO_3$ (acetonitrile) as reference electrode). The spectroelectrochemical and coulometric experiments were done in 0.1 M $TBAPF_6$ acetonitrile solutions. The whole setup, which allows for simultaneous electrolysis and UV–vis spectral recording, was purged with Ar and thermostated to -30 ± 2 °C. Electrolysis was performed over a platinum-net. A second platinum-net separated by a frit glass was used as a counter electrode, and $Ag/AgNO_3$ (AcN) was used as reference electrode. Electronic spectra were collected on a diode-array Hewlett-Packard 8453 instrument in the range 190–1100 nm. Due to the electrochemically irreversible behavior under CV conditions (see results), the redox potentials of the compounds were determined by potentiometric titration. In a typical experiment, the solution was electrolyzed at sufficiently high potential (ca. 300 mV higher than the anodic peak potentials registered by CV), in several anodic steps. Between consecutive oxidation periods, the solution was allowed to equilibrate and the open-circuit potential (E_{oc}) together with the UV–vis spectrum were recorded. Redox potentials and UV–vis spectra of the reduced and oxidized species were then obtained by global analysis and fitting to a simple one-electron Nernst behavior (see results).

Electrogenerated samples (ca. 1 mM in acetonitrile/0.1 M $TBAPF_6$) were transferred via syringe (the solutions being in contact with glass and Teflon exclusively) for EPR analysis. The electrochemical conversion to the one-electron oxidized forms of complexes was better than 97% in agreement with spin quantitations via double integration of the corresponding EPR spectra. X-band EPR spectra were recorded on a Bruker ESP 300 spectrometer equipped with an Oxford Instruments ESR 910 helium-flow cryostat with an ITC 503 temperature controller. The solution spectra were simulated with the programs GFIT and S32 of the ESIM package (by E.B.).

Magnetically perturbed Mössbauer spectra were recorded on ^{57}Fe enriched material (frozen solutions in acetonitrile, same concentration and preparation procedures as for the EPR determinations). Data were recorded on an alternating constant-acceleration spectrometer. A constant sample temperature was maintained with an Oxford Instruments Variox or an Oxford Instruments Mössbauer-Spectromag 2000 Cryostat. The latter is a split-pair superconducting magnet system for applied fields up to 8 T in which the sample temperature can be varied between 1.5 and 250 K with the field of the sample oriented perpendicular to the γ-beam. The $^{57}Co/Rh$ source (1.8 GBq) was positioned at room-temperature inside the gap of the magnet system at a zero-field position. Reported isomer shifts (δ) are referenced versus iron metal at 300 K.

Table 1. Crystallographic Data for 4·0.5 MeCN·0.25 Et_2O

chem. formula	$C_{24}H_{41}BF_6Fe_2N_{9.5}O_{5.25}P$
fw	1597.13
space group	*Fdd2, No. 43*
a, Å	32.721(4)
b, Å	49.518(5)
c, Å	8.6090(8)
V, Å^3	4818.9(7)
Z	16
T, K	100(2)
ρ calcd, g cm^{-3}	1.551
diffractometer used	Siemens SMART
refl. collected/θ_{max}	38686/68.22
unique refl./$I > 2\sigma(I)$	12012/8899
no. of params/restraints	506/1
μ(MoKα), cm^{-1}	9.59
R1 ^{a}/goodness of fit ^{b}	0.0541/1.034
w$R2$ ^{c} ($I > 2\sigma(I)$)	0.1063

^{a} $I > 2\sigma(I)$. R1 $= \Sigma||F_o| - F_c||/\Sigma|F_o|$. ^{b}GooF $= [\Sigma[w(F^2_o - F^2_c)^2]/(n - p)]^{1/2}$. ^{c}w$R2 = [\Sigma[w(F^2_o - F^2_c)^2]/[\Sigma[w(F^2_o)^2]]^{1/2}$, where $w = 1/\sigma^2(F^2_o) + (aP)^2 + bP$, $P = (F^2_o + 2F^2_c)/3$.

Temperature-dependent (2–290 K) magnetic susceptibility data were recorded on a SQUID magnetometer (MPMS Quantum Design) in an external field of 1.0 T. The experimental susceptibility data were corrected for underlying diamagnetism by use of tabulated Pascal's constants.

Magnetic susceptibility data were analyzed on the basis of a spin-Hamiltonian description of the spin-coupled dimer system by using

$$\hat{H} = -2J\hat{S}_1\hat{S}_2 + \sum_{i=1,2} D_i[\hat{S}^2_{zi} - {}^1/_3 S_i(S_i + 1) + E_i/D_i(\hat{S}^2_{xi} - \hat{S}^2_{yi})] + \mu_B \mathbf{B}g_i\hat{S}_i \quad (1)$$

where $\hat{S}_i$, $i = 1,2$, are the spins of the iron ions in the dimers, D_i, E_i, $\mathbf{g}_i$ are the local axial and rhombic zero-field parameters and g values, respectively, and J represents the exchange coupling constant. EPR spectra and magnetic Mössbauer spectra were simulated by using the corresponding effective Hamiltonian for the total spin ground state

$$\hat{H} = D[\hat{S}^2_z - {}^1/_3 S(S + 1) + E/D(\hat{S}^2_x - \hat{S}^2_y)] + \mu_B \mathbf{B}g\hat{S} \quad (2)$$

For the calculation of magnetic Mössbauer spectra eq 2 was accomplished using the usual nuclear Hamiltonian. The magnetic Mössbauer spectra are simulated in the limit of slow paramagnetic relaxation. Zero-field Mössbauer spectra recorded from solid material (fast relaxation at 80 K) were fitted with Lorentzian line doublets.

X-ray Crystallographic Data Collection and Refinement of the Structure. A brown single crystal of **4**(PF_6)·0.5CH_3CN·0.25Et_2O was coated with perfluoropolyether, picked up with a glass fiber and immediately mounted in the nitrogen cold stream to prevent loss of solvent. Intensity data were collected at 100 K using graphite monochromated Mo–Kα radiation ($\lambda = 0.710~73$ Å). Final cell constants were obtained from a least-squares fit of a subset of 6395 reflections and are summarized in Table 1. Data collection was performed on a Siemens SMART diffractometer system by a hemisphere run taking frames at 0.3° in ω. A semiempirical absorption correction using the program SADABS was applied giving minimal and maximal transmission factors of 0.611 and 0.862. Crystallographic data of the compound are listed in Table 1. The Siemens ShelXTL[20] software package was used for solution, refinement and artwork of the structure. The structure was readily solved by direct methods and difference Fourier techniques. All non-hydrogen atoms except some atoms in disordered parts were refined anisotropically and hydrogen atoms were placed at calculated positions and refined as riding atoms with isotropic displacement

(20) (a) *Shel*XTL V.5; Siemens Analytical X-ray Instruments, Inc.: Madison, WI, 1994. (b) Sheldrick, G. M. *Shel*XTL-97; Universität Göttingen: Göttingen, Germany, 1997.

Table 2. X-ray Absorption near Edge Spectroscopic Data for Complexes **2**, **2**ᵒˣ, **5**, **5**ᵒˣ at 20 K

complex	edge position, eV[a]	pep, eV[b]	I(pep)[c]	fwhm(pep), eV[d]
2	7121.81	7112.18	0.024	1.48
		7113.42	0.029	1.52
2ᵒˣ	7123.15	7111.76	0.023	1.50
		7113.17	0.027	2.34
5	7121.82	7112.22	0.018	1.37
		7113.53	0.029	1.56
5ᵒˣ	7121.98, 7125.11	7111.67	0.028	1.38
		7113.00	0.024	1.92

[a] Edge position taken from the second maximum of the derivative. [b] Two pre-edge peaks. [c] Relative intensity of the pre-edge peaks. [d] Full width at half-maximum.

parameters. The PF_6^- anion and solvent molecules of crystallization were found to be disordered. Split atom models were used to account for the disorder, details are given in the Supporting Information.

X-ray Absorption Spectroscopy (XAS, EXAFS). XAS measurements at 20 K were performed at the EMBL bending magnet beam line D2 (DESY, Hamburg, Germany). The experimental setup comprises a Si(111) double crystal monochromator, a focusing mirror, a closed-cycle cryostat (modified Oxford Instruments), and a 13-element Ge solid-state detector. The intensity of the radiation on the sample was monitored by an ionization chamber. The radiation transmitting the sample has been utilized for the energy calibration of each individual scan by means of Bragg reflections of a static Si(220) crystal.[21] The energy resolution was better than 1.8 eV. A data range from 2.7 $Å^{-1}$ to 14.2 $Å^{-1}$ was used for the structural refinement of all samples. The EXPROG program package[22] was applied for data reduction and averaging. The EXAFS fine structures were analyzed with Excurve 98.[23] Fermi energy, metal-neighbor distances as well as corresponding Debye–Waller factors were refined as indicated in Table 8. The initial model was defined by the crystal structures for the compounds with both metals in the oxidation state III. The refinement was performed using single scattering. Multiple scattering within a unit comprising both metals, the bridge carboxylates and oxo ligand did not improve significantly the fit index. The significance of individual contributions (i.e., the metal–metal contribution) has been probed by the F-test[24] implemented by Michalowicz et al..[25] The fit of the pre-edge-peak (pep) was performed with WinXAS[26] refining the position, full width at half-maximum height (fwhm) and intensity of the peak.

Quantum Chemical Calculations. All calculations reported in this paper were performed with the program package ORCA.[27] The geometry optimizations were carried out at the BP86 level[28] of DFT. This functional has repeatedly proved to be reliable in predicting accurate structures of transition metal complexes. We employed the all-electron Gaussian basis sets reported by the Ahlrichs group.[29] For the metals, the nitrogens and the oxygen atoms accurate triple-ζ valence basis sets with one set of polarization (TZV(P)) functions were used.[29b] The carbon and hydrogen atoms were described by a slightly smaller polarized split-valence SV(P) basis set that is of double-ζ quality in the valence region and contains a polarizing set of d-functions on the non-hydrogen atoms.[29a] The auxiliary basis sets used to fit the electron

density were taken from the TurboMole library[30] and were chosen to match the orbital basis.

The SCF calculations were of the spin-polarized type and were tightly converged (10^{-7} Eh in energy, 10^{-6} in the density change and 10^{-6} in maximum element of the DIIS[31] error vector). High spin optimizations were performed using starting coordinates based on the crystal structures when available. The broken symmetry (BS) states were optimized employing the converged high spin geometries as initial guesses. In all cases the geometries were considered converged after the energy change was less than 10^{-5} Eh, the gradient norm and maximum gradient element were smaller than 5×10^{-4} Eh/Bohr and 10^{-3} Eh/Bohr, respectively, and the root-mean square and maximum displacement of atoms were smaller than 10^{-3} Bohr.

Single point calculations on the optimized BS geometries with the B3LYP functional[28,32] where carried out in order to predict EPR[33] and Mössbauer[34] spectral parameters. For the quadrupole moment of ^{57}Fe the value 0.15 barn was used in place of the more common value of 0.2 barn.[35] This choice is based on the finding that the B3LYP DFT calculations tend to overestimate the quadrupole splitting and there is considerable uncertainty in the literature about the best choice of the quadrupole moment of the iron nucleus. In these calculations, the same basis sets were used as in the geometry optimizations except for the metal basis which was the triply polarized "Core Properties" (CP(PPP)) basis described earlier.[34] Special care was taken in the numerical integration procedure to accurately integrate the electron density in the core region as is required for the prediction of Mössbauer isomer shifts.[34]

BS-type spin unrestricted solutions were analyzed via the corresponding orbital transformation[36,37] and the spin unrestricted natural orbitals. Note that in the latter two cases, the orbitals do not have a well defined orbital energy. In the figures showing such orbitals, we therefore do not give orbital energies explicitly. It is the occupation and spin-coupling patterns that are our main interest.

Results and Discussion

Synthesis of Complexes. Versatile synthetic routes to complexes containing the (μ-oxo)bis(μ-acetato)diiron(III) core have been successfully employed in the past. (a) Hydrolysis of mononuclear precursors, [(tridentate ligand)$Fe^{III}Cl_3$] in aqueous sodium acetate solution or, alternatively, (b) by ′spontaneous self-assembly′ from Fe(ClO₄)₃·10H₂O, NaOAc·3H₂O and Na-(HBpz₃) in H₂O. [1–4] Thus, complexes [([9]aneN₃)₂Fe₂(μ-O)(μ-CH₃CO₂)₂]²⁺ (**1**), [Me₃[9]aneN₃)₂Fe^{III}₂(μ-O)(μ-CH₃CO₂)₂]²⁺ (**2**), and [([9]aneN₃)Fe^{III}(μ-O)(μ-CH₃CO₂)₂Cr^{III}(Me₃[9]aneN₃)]²⁺ (**5**) have been prepared following route (a), whereas complex [(tpb)₂Fe^{III}₂(μ-O)(μ-CH₃CO₂)₂] (**3**) has originally[1] been synthesized by route (b). It is also possible to use route a) for the synthesis of **3**.[17] Thus, hydrolysis of [(tpb)Fe^{III}Cl₃](NEt₄) in aqueous solution of sodium acetate at 20 °C yields **3** in good yields.

(21) Pettifer, R. F.; Hermes, C. *J. Appl. Crystal.* **1985**, *18*, 404.
(22) Nolting, H.-F.; Hermes, C. EXPROG: EMBL, EXAFS data analysis and evaluation program package 1992.
(23) Binstead, N.; Strange, R. W.; Hasnain, S. S. *Biochemistry* **1992**, *31*, 12 117.
(24) Joyner, R. W.; Martin, K. J.; Mehan, P. *J. Phys.* **1987**, *C20*, 4005.
(25) Michalowicz, A.; Provost, K.; Larvelle, S.; Mimouni, A.; Vlaic, G. J. *J. Synchroton Rad.* **1999**, *6*, 233.
(26) Ressler, T. *J. Synchroton Rad.* **1998**, *5*, 118.
(27) Neese, F. Orca—an ab Initio DFT and Semiempirical Electronic Structure Package. Version 2.2, Revision 14, Max-Planck-Institut für Strahlenchemie, Mülheim, Germany, May 2002.
(28) (a) Becke, A. D. *J. Chem. Phys.* **1988**, *84*, 4524. (b) Perdew, J. P. *Phys. Rev. B.* **1986**, *33*, 8822.
(29) (a) Schäfer, A.; Horn, H.; Ahlrichs, R. *J. Chem. Phys.* **1992**, *97*, 2571. (b) Schäfer, A.; Huber, C.; Ahlrichs, R. *J. Chem. Phys.* **1994**, *100*, 5829.
(30) (a) Basis sets were obtained from the ftp server of the quantum che+mistry group at the University of Karlsruhe (Germany) under http://www.che-mie.uni-karlsruhe.de/PC/TheoChem/. (b) Eichhorn, K.; Treutler, O.; Öhm, H.; Häser, M.; Ahlrichs, R. *Chem. Phys. Lett.* **1995**, *240*, 283.
(31) (a) Pulay, P. *Chem. Phys. Lett.* **1980**, *73*, 393. (b) Pulay, P. *J. Comput. Chem.* **1992**, *3*, 556.
(32) (a) Lee, C.; Yang, W.; Parr, R. G. *Phys. Rev. B* **1988**, *37*, 785. (b) Becke, A. D. *J. Chem. Phys.* **1993**, *98*, 5648.
(33) (a) Neese, F.; Solomon, E. I. *Inorg. Chem.* **1998**, *37*, 6568. (b) Neese, F. *J. Chem. Phys.* **2001**, 11 080 (c) Neese, F. *Int. J. Quantum Chem.* **2001**, *83*, 104. (d) Neese, F. *J. Phys. Chem. A* **2001**, *105*, 4290. (e) Neese, F. *J. Chem. Phys.* **2003**, *117*, 3939.
(34) Neese, F. *Inorg. Chim. Acta* **2002**, *337*, 181.
(35) Dufek, P.; Blaha, P.; Schwarz, K. *Phys. Rev. Lett.* **1995**, *75*, 3545.
(36) (a) Amos, A. T.; Hall, G. G. *Proc. R. Soc. Ser. A* **1961**, *263*, 483. (b) King, H. F.; Stanton, R. E.; Kim, H.; Wyatt, R. E.; Parr, R. G. *J. Chem. Phys.* **1967**, *47*, 1936.
(37) Ghosh, P.; Bill, E.; Weyhermüller, T.; Neese, F.; Wieghardt, K. *J. Am. Chem. Soc. 125*, 1293.

Table 3. Summary of Structural, Mössbauer Spectral, and Magnetic Properties of Complexes **1**−**5** Containing the $\{Fe^{III}(\mu\text{-}O)(\mu\text{-}CH_3CO_2)_2M^{III}\}^{2+}$ Core (M = Fe^{III} or Cr^{III})

	1	2	3	4^a	5^c
Fe—O—M, deg	118.7(4)	119.7(1)	123.6(1)	121.4(1)	121.1(4)
Fe—O$_{oxo}$, Å	1.77, 1.80	1.80	1.78	1.80, 1.79	1.79
Fe—N cis to μ-oxo, Å	2.17	2.20	2.15	2.14, 2.20	2.20
Fe—N trans to μ-oxo, Å	2.20	2.27	2.19	2.20, 2.27	2.24
Fe··M, Å	3.06	3.12	3.15	3.13	3.13
Fe—O$_{carboxylate}$, Å	2.04	2.03	2.04	2.07, 2.02	2.05
S$_t$^{b}	0	0	0	0	1
J, cm^{-1} ^{e}	−111^d	−119	−121	−120	−137
δ, mm/s (80 K) ^{f}	0.46 ^{d}	0.47	0.52	0.52, 0.47	0.52 (4.2 K)
ΔE_Q, mm/s (80 K) ^{g}	1.60 ^{d}	1.50	1.60	1.67, 1.51	−2.00 (4.2 K)
reference	2	3, 4	1	this work	14, 15

^{a} The first number pertains to the (tpb)Fe^{III}− and the second to the (Me$_3$[9]aneN$_3$)Fe^{III} moiety. ^{b}Ground state. ^{c}Bond distances are for the ([9]aneN$_3$)FeO$_3$ moiety only. ^{d}This work. ^{e}Exchange coupling constant $H = -2J$ S$_1$·S$_2$. ^{f}Mössbauer isomer shift vs α-Fe at 298 K. ^{g}Mössbauer quadrupole splitting.
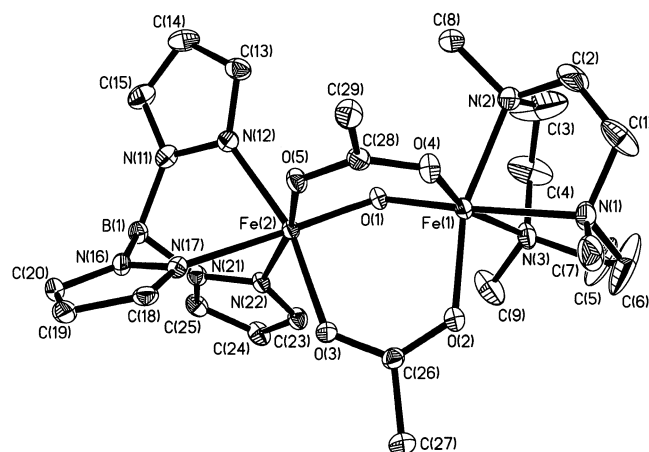
Figure 1. Structure of the monocation in crystals of **4**(PF$_6$)·0.5CH$_3$CN·0.25(C$_2$H$_5$)$_2$O.

Interestingly, the asymmetrically ligated dinuclear species [(tpb)Fe^{III}(μ-O)(μ-CH$_3$CO$_2$)$_2$Fe^{III}(Me$_3$[9]aneN$_3$)]$^+$ (**4**) is available via route (a) in excellent yields by hydrolysis of an equimolar mixture of (Me$_3$[9]aneN$_3$)Fe^{III}Cl$_3$ and [(tpb)Fe^{III}Cl$_3$]-(NEt$_4$) in aqueous sodium acetate solution. Its electronic spectrum in acetonitrile solution displays absorption maxima at 342 (7.7 × 10^3), 374 (5.1 × 10^3)sh, 418(950)sh, 466 (1.35 × 10^3), 498(880), 546(150), 745 nm (ϵ = 200 L mol^{-1} cm^{-1}). The X-ray crystal structure determination of **4**(PF$_6$)·0.5CH$_3$CN·0.25(C$_2$H$_5$)$_2$O confirms the presence of the asymmetrically ligated two high-spin ferric ions ((tpb)Fe^{III} and (Me$_3$[9]aneN$_3$)Fe^{III}) which are bridged by an oxo- and two μ-acetato groups (Figure 1). Table 3 summarizes important bond lengths; full details of the structure determination are available in the Supporting Information.

From temperature-dependent (3−300 K) magnetic susceptibility measurements (Figure S1) it has been established that **4**(PF$_6$) contains two antiferromagnetically coupled high spin ferric ions (S$_{Fe}$ = $^5/_2$) yielding a diamagnetic ground-state S$_t$ = 0 with a coupling constant, J, of −120(5) cm^{-1}, g = 2.0 (fixed) and χ_{TIP} = 126 × 10^{-6} emu ($H = -2J$ S$_1$·S$_2$; S$_1$ = S$_2$ = $^5/_2$). This value of J is within experimental error the same as in **1**, **2**, and **3** and many other complexes containing the (μ-oxo)bis(μ-carboxylato)diiron(III) core (Table 3). The magnetic properties of **1** have been redetermined here (Figure S2). The antiferromagnetic coupling constant is found to be −111(5) cm^{-1} instead of −84(1) cm^{-1} reported in ref 3,4. The discrepancy arises from the limited temperature range (80−298 K) employed previously.

Note that complex **4** contains two uniquely coordinated ferric ions: it has a (Me$_3$[9]aneN$_3$)Fe^{III} *and* a (tpb)Fe^{III} moiety. It is therefore possible to selectively label both ferric ions in **4** with ^{57}Fe and generate the isotopomers [(tpb)^{57}Fe^{III}(μ-O)(μ-CH$_3$CO$_2$)$_2$Fe^{III}(Me$_3$[9]aneN$_3$)]$^+$ (**4a**) and [(tpb)Fe^{III}(μ-O)(μ-CH$_3$CO$_2$)$_2$^{57}Fe^{III}(Me$_3$[9]aneN$_3$)]$^+$ (**4b**) by using route a). Hydrolyses of a mixture of ^{57}Fe enriched [(tpb)^{57}FeCl$_3$](NEt$_4$) and not enriched (Me$_3$[9]aneN$_3$)FeCl$_3$ in one case and of a mixture of [(tpb)FeCl$_3$](NEt$_4$) and ^{57}Fe enriched (Me$_3$[9]aneN$_3$)^{57}FeCl$_3$ in the other instance yield **4a** and **4b**, respectively. The absence of significant scrambling between enriched and nonenriched sites in **4a**, **4b**, respectively, has been unequivocally proven by their ^{57}Fe-Mössbauer spectra. The isomer shift and quadrupole splitting parameters of the (Me$_3$[9]aneN$_3$)Fe^{III} and the corresponding (tpb)Fe^{III} moieties are slightly different.

The heterodinuclear species **5** has been prepared previously;[14] it has been prepared via route b) where an equimolar mixture of [([9]aneN$_3$)FeCl$_3$] and [(Me$_3$[9]ane)CrBr$_3$] has been hydrolyzed in an aqueous solution of sodium acetate. **5** possesses an S$_t$ = 1 ground state which is attained via intramolecular antiferromagnetic coupling (J = −137 cm^{-1}) between a high spin ferric ion and a chromium(III) ion. The crystal structure of **5**(ClO$_4$)$_2$·H$_2$O has also been reported.[14]

We have discovered that it is possible to oxidize complex **1** chemically by one electron affording solid [([9]aneN$_3$)Fe^{IV}(μ-O)(μ-CH$_3$CO$_2$)$_2$Fe^{III}([9]aneN$_3$)](PF$_6$)$_{1.5}$(SbCl$_6$)$_{1.5}$·CH$_2$Cl$_2$ (**1^{ox}**-(PF$_6$)$_{1.5}$(SbCl$_6$)$_{1.5}$·CH$_2$Cl$_2$). Thus, from an equimolar mixture of **1**(PF$_6$)$_2$ and [Ṅ R$_3$][SbCl$_6$], where R represents 2,4-dibromophenyl in cold CH$_2$Cl$_2$ at −30 °C deep red microcrystals of [**1^{ox}**]-(PF$_6$)$_{1.5}$(SbCl$_6$)$_{1.5}$·CH$_2$Cl$_2$ were obtained. The electrospray mass spectrum (positive ion) exhibits the {**1^{ox}**}$^{3+}$ peak at $m/3$ = 168.0 whereas the negative ion mode displays signals at m/z = 145.0 and 331 corresponding to the anions PF$_6^-$ and SbCl$_6^-$, respectively. This material is not stable at room temperature. It may be stored at −40 °C in the absence of any reducing agent for a day.

Similarly, from the analogous reaction of **5**(PF$_6$)$_2$ in CH$_2$Cl$_2$ at −30 °C with one equivalent of [Ṅ R$_3$]SbCl$_6$ microcrystals of [([9]aneN$_3$)Fe^{IV}(μ-O)(μ-CH$_3$CO$_2$)$_2$Cr^{III}(Me$_3$[9]aneN$_3$)](PF$_6$)$_2$-(SbCl$_6$)·2CH$_2$Cl$_2$·2CH$_3$CN (**5^{ox}**(PF$_6$)$_2$(SbCl$_6$)·2CH$_2$Cl$_2$·2CH$_3$-CN) were obtained. Again, the ESI mass spectrum (pos. ion) showed the correct {**5^{ox}**}$^{3+}$ peak at $m/3$ = 180.8. This material must also be stored at −40 °C because the complex is not stable—even in the solid state—at room temperature. The fact that the ferric ion in **5** is oxidized and not the Cr(III) ion is
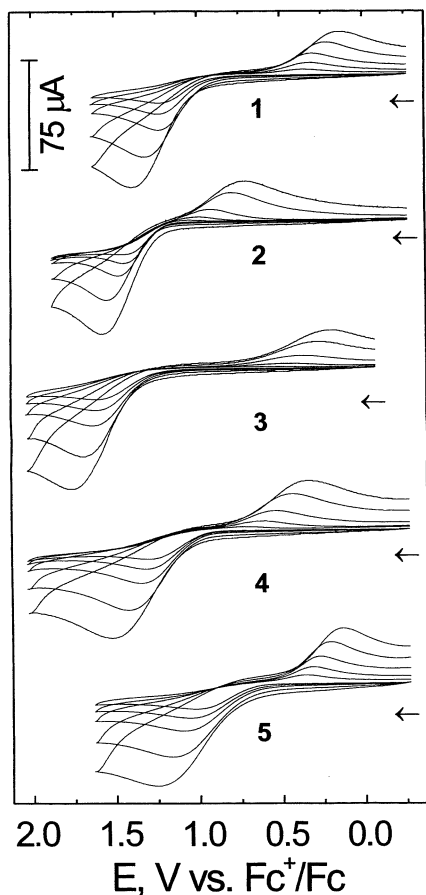
Figure 2. Cyclic voltammograms of complexes **1**−**5** in acetonitrile (0.10 M [TBA]PF$_6$ supporting electrolyte) at 25 ± 2 °C (conditions: glassy carbon working electrode; scan rates 50, 100, 200, 500, and 1000 mV s^{-1}). Potentials are referenced vs the Fc$^+$/Fc couple and the arrows indicate the direction of the scans.

unequivocally established by the Mössbauer spectra of **5** and **5**^{ox} (see below).

Spectro- and Electrochemistry of Complexes. The cyclic voltammograms of **2** and **3** in CH$_3$CN and CH$_2$Cl$_2$ solutions containing 0.10 M [N(n-Bu)$_4$]PF$_6$ as supporting electrolyte at 20 °C have previously been recorded in the potential range +0.3 to −1.7 V vs Fc$^+$/Fc (Fc$^+$ = ferrocenium, Fc = ferrocene).[1,2,4] In the following, all redox potentials are referenced vs the Fc$^+$/Fc couple. In both cases, a quasireversible and an irreversible one-electron reduction wave, respectively, have been observed at quite cathodic potentials yielding a mixed-valent complex with an {Fe^{II}(μ-O)bis(μ-carboxylato)$_2$Fe^{III}}$^+$ core (S$_t$ = $^1/_2$) and the unstable diiron(II) analogues. The former have been characterized by EPR spectroscopy.[4]

When the potential range is expanded to more anodic potentials (∼1.8 V vs Fc$^+$/Fc) at 25 °C we observe an oxidation peak, $E_{p,ox}$, at ∼1.3 V and, upon reversal of the scan, a new reduction peak, $E_{p,red}$, at ∼0.5 V for complexes **1**−**5** as is shown in Figure 2. The results are summarized in Table 4.

The difference between the two peaks, ΔE, is much larger at ∼1.0 V than is expected for a Nernstian reversible one-electron-transfer wave (∼60 mV). ΔE is temperature and scan rate dependent. These features are normally associated with irreversible processes. Alternatively, strongly kinetically inhibited heterogeneous electron transfer processes at the working electrode (glassy carbon) are also expected to show similar

Table 4. Redox Potentials for the One-electron Oxidation Processes of Complexes **1**−**5** at 25 °C vs the Ferrocenium/Ferrocene (Fc$^+$/Fc) Couple in CH$_3$CN (0.10 M [N(n-Bu)$_4$]PF$_6$)

complex	$E_{p,ox}$, V [a]	$E_{p,red}$, V [b]	ΔE, V [c]	$E^{ox}_{1/2}$, V [d]	$E°$, V [e,f]
1	1.23	0.30	0.93	0.77	0.70
2	1.48	0.92	0.56	1.20	1.08
3	1.64	0.37	1.27	1.00	1.05
4	1.35	0.54	0.81	0.95	0.91
5	1.10	0.27	0.83	0.68	0.58

[a] Peak potential of oxidation at +25 °C, scan rate 200 mV s^{-1}. [b] Peak potential of reduction at +25 °C at scan rate 200 mV s^{-1}. [c] $\Delta E = (E_{p,ox} - E_{p,red})$, at scan rate 200 mV s^{-1}. [d] $(E_{p,ox} + E_{p,red})/2 = E^{ox}_{1/2}$ assuming a kinetically hindered reversible one-electron-transfer process. [e] Redox potentiometric titration (see text) at −25 °C. [f] The redox potential for [NR$_3$](SbCl$_6$) (R = 2,4- dibromophenyl) is reported at +1.14 V (Connelly, N. G.; Geiger, W. E. *Chem. Rev.* **1996**, *96*, 877).
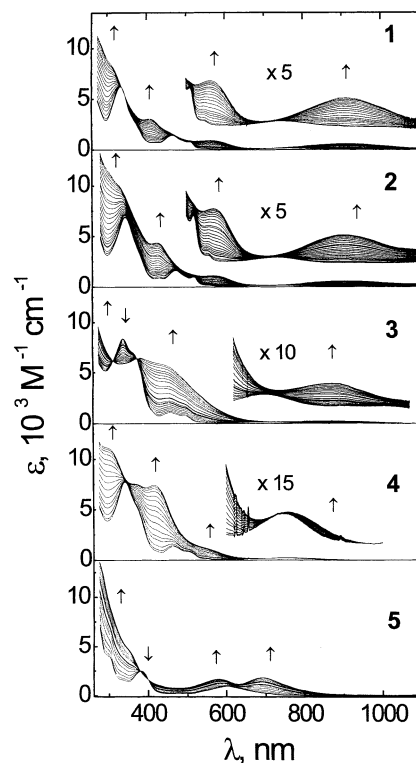

Figure 3. Controlled potential spectroelectrochemistry of the one-electron oxidation of complexes **1**−**5** at −20 °C in acetonitrile (0.10 M [TBA]PF$_6$). The arrows indicate the observed spectral changes during the oxidation.

behavior. That the latter is probably true is born out by the observation that at lower temperatures (−25 °C) ΔE increases, and the overall behavior does not approach that of a simple reversible one-electron process even at fast scan rates of ∼1.0 V s^{-1}.

Controlled potential coulometry of complexes **1**−**5**, at −25 °C and a fixed potential of 1.8 V in CH$_3$CN solution (0.10 M [TBA]PF$_6$) revealed that a single electron per dinuclear unit is removed (n = 1.0 ± 0.1). Electronic spectral changes during the coulometric one-electron oxidation of **1**−**5** have been recorded. The results are shown in Figure 3 and are summarized in Table 5. Interestingly, for complexes **1**, **3**, **4**, and **5** at least one, well-defined isosbestic point is observed, which indicates the absence of side reactions or decomposition. As it turned out the one-electron oxidized species [**1**^{ox}]−[**5**^{ox}] are stable on the minutes-to-hours time scale at −25 °C. At temperatures (> −20 °C) a slow decomposition is observed. We have shown that at −25 °C, the one-electron oxidized forms of complexes

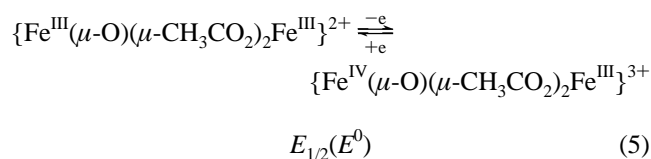**Table 5.** Electronic Spectra of Electrochemically Generated Oxidized Complexes (CH$_3$CN, 0.10 M [TBA]PF$_6$)

complex	λ_{max}, nm (ϵ, M^{-1} cm^{-1})
1^{ox}	315(8.6 × 10^3)sh, 566(1.0 × 10^3), 912(650)
2^{ox}	330(10.1 × 10^3)sh, 571(1.1 × 10^3), 904(600)
3^{ox}	388(6.5 × 10^3), 445(6.0 × 10^3)sh, 868(250)
4^{ox}	297(11.3 × 10^3), 364(7.6 × 10^3), 416(7.6 × 10^3), 552(1.2 × 10^3)sh, 759(210)
5^{ox}	270(1.4 × 10^4), 350(4.8 × 10^3)sh, 579(1.8 × 10^3), 692(1.9 × 10^3)

Table 6. X-band EPR Spectral Data for Electrochemically Generated One-Electron Oxidized Form of **1**–**5**

complex	S^a	g_x	g_y	g_z	E/D^b
1^{ox}	$^3/_2$ (65%)	1.990	1.990	1.975	0.028
	$^1/_2$ (35%)	2.411	1.921	1.685	
2^{ox}	$^3/_2$	1.971	1.971	1.971	0.025
3^{ox}	$^3/_2$	1.980	1.980	1.980	0.077
4^{ox}	$^3/_2$	2.000	2.000	1.975	0.050
5^{ox}	$^1/_2$	1.976	1.938	1.914	

^{a} Ground state. ^{b}Rhombicity factor.

can be electrochemically reduced at +0.35 V yielding the starting complexes **1**–**5** in 98% yield. These experiments clearly show that the complexes **1**–**5** are cleanly one-electron oxidized at −20 °C without detectable decomposition. At higher temperatures, these species are readily reduced probably via suicidal H atom abstraction from the ligand.

Recovery of the starting materials (>97%) from the electrochemically oxidized forms was also achieved in a stoichiometric fashion by addition of reducing agents such as ferrocene or 9,10-dihydro-*N*-methyl-acridine as has been established by UV−vis spectroscopy, eqs 3 and 4.

$$[\mathbf{1}^{ox} - \mathbf{5}^{ox}] + Cp_2Fe \rightarrow [\mathbf{1} - \mathbf{5}] + [Cp_2Fe]^+ \quad (3)$$

$$(4)$$
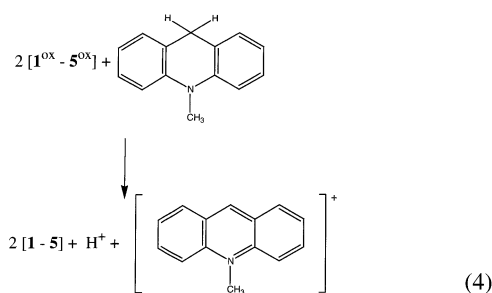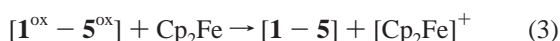
The redox potentials, $E_{1/2}(E°)$, eq 5 have been determined experimentally in the following manner. Compounds **1**−**5** were coulometrically stepwise oxidized using

$$\{Fe^{III}(\mu\text{-O})(\mu\text{-CH}_3CO_2)_2Fe^{III}\}^{2+} \underset{+e}{\overset{-e}{\rightleftharpoons}}$$

$$\{Fe^{IV}(\mu\text{-O})(\mu\text{-CH}_3CO_2)_2Fe^{III}\}^{3+}$$

$$E_{1/2}(E^0) \quad (5)$$

the same experimental conditions (acetonitrile, 0.10 M [TBA]-PF$_6$, −20 °C) as in the cyclic voltammetry experiments at a fixed potential of 1.3 V. The electronic spectra and open-circuit potentials, E, which were stable for several minutes were recorded after each step. Factor analysis of the spectroscopic data and fitting to the Nernst eq 6 was performed.

$$E = E_0 + \frac{R.T.}{nF} \ln \frac{[X^{ox}]}{[X^{red}]}, \qquad [X^{ox}] + [X^{red}] = [X]_{tot} \quad (6)$$

The experimental fitting procedure was done both in the anodic (oxidation of **1** − **5**) and the cathodic direction (reduction of **1**^{ox}−**5**^{ox}) where the two E_0 values obtained were found to be in excellent agreement. Table 4 summarizes these potentials. The potentials obtained in this fashion are remarkably similar to $E_{1/2}$ values which were calculated from the cyclic voltammograms

by using the relation $E_{1/2} = (E_{p,ox} + E_{p,red})/2$. This is taken as further evidence that the cyclic voltammograms in Figure 2 do not represent chemical irreversibility but rather electrode kinetic complications.

From the data for $E°$ ($E_{1/2}$) in Table 4, it follows that complexes containing an ([9]aneN$_3$)Fe^{III}O$_3$ octahedral core are the easiest to oxidize; i.e., **1**, **4**, and **5**. Species containing two (Me$_3$[9]aneN$_3$)Fe^{III} or two (tpb)Fe^{III} fragments as in **2** and **3**, respectively, are more difficult to oxidize by ∼300 mV. For the asymmetric complex **4** the Mössbauer data in Table 7 then imply that the (Me$_3$[9]aneN$_3$)Fe fragment is oxidized in **4**^{ox} and not the (tpb)Fe^{III} fragment which retains its oxidation state. The similarity of $E_{1/2}$ values for **1** and **5** implies that the ([9]aneN$_3$)-Fe core is oxidized and not the (Me$_3$[9]aneN$_3$)Cr part.

The electronic spectra of the oxidized forms of **1**, **2**, **3**, and **4** (Figure 3, Table 5) display each a new weak absorption maximum at wavelengths >750 nm which we tentatively assign to class II mixed-valent charge-transfer bands (Fe^{III}Fe^{IV}); in **5**^{ox} such an absorption maximum is not observed. It is gratifying that the spectra of electrochemically generated **1**^{ox} and **5**^{ox} are within experimental error identical with CH$_3$CN solutions of solid [**1**^{ox}](PF$_6$)$_{1.5}$(SbCl$_6$)$_{1.5}$·CH$_2$Cl$_2$ and **5**^{ox}(PF$_6$)$_2$(SbCl$_6$)·2CH$_2$Cl$_2$·2CH$_3$CN, respectively. These observations point to class II behavior of the mixed-valent complexes **1**^{ox}−**4**^{ox}, where the oxidation states of III and IV of the iron ions are localized.

X-Band EPR Spectroscopy. Complexes **1**−**4** are EPR-silent as is **5** due to their integer spin ground states of S$_t$ = 1 with large zero-field splitting (zfs) and/or S$_t$ = 0. In contrast, the electrochemically generated one-electron oxidized forms of these complexes are EPR-active. Figure 4 shows the X-band EPR spectra of **2**^{ox}, **3**^{ox}, and **4**^{ox} at 2−10 K and Table 6 summarizes the results. These spectra with effective g values $g_x \approx g_y \approx 4$ and $g_z \approx 2$ are typical for a spin quartet ground state (S = $^3/_2$) with large zfs ($D \gg h\nu$). In contrast, the spectrum of **5**^{ox} at 10 K shown in Figure 5 displays a rhombic signal at $g \approx 2.0$ (1.976, 1.938, 1.914) typical for an S = $^1/_2$ ground state. The ground state of S = $^3/_2$ is attained via an intramolecular antiferromagnetic coupling between an Fe^{IV} ion (S$_{Fe}$ = 1) and a high spin ferric ion (S$_{Fe}$ = $^5/_2$) in **2**^{ox}, **3**^{ox}, and **4**^{ox}. In **5**^{ox} such intramolecular antiferromagnetic coupling between an Fe^{IV} ion (S$_{Fe}$ = 1) and an Cr^{III} ion (S$_{Cr}$ = $^3/_2$) affords the observed S = $^1/_2$ ground state.

The X-band EPR spectrum of **1**^{ox} shown in Figure 6 is more complicated and, in fact, quite intriguing because it consists of two subspectra. Deconvolution and simulation clearly establishes that an S = $^3/_2$ and an S = $^1/_2$ species (ratio 65:35%) is present at 10 K. This pattern of the spectrum is reproducible and independent of the concentration of complex **1**^{ox}. It may indicate that the ([9]aneN$_3$)Fe^{IV}O$_3$ site exists in a temperature-dependent spin equilibrium: S$_{Fe}$ = 2 (high spin Fe^{IV}) and S$_{Fe}$ = 1 (low

Table 7. Experimental Spin Hamiltonian and Hyperfine Parameters for the Oxidized Species **1**ox−**5**ox at 4.2 K

	1ox				**2**ox		**3**ox		**4**ox		**5**ox
	Fe^{III}	Fe^{IV} (S = 1)	Fe^{III}	Fe^{IV} (S = 2)	Fe^{III}	Fe^{IV}	Fe^{III}	Fe^{IV}	Fe^{III}	Fe^{IV}	Fe^{IV}
S_t [a]	$^3/_2$		$^1/_2$		$^3/_2$		$^3/_2$		$^3/_2$		$^1/_2$
D, cm^{-1} [b]	8.05				6.4		5.3		3.83	3.74	
E/D [c]	0.010				0.025		0.077		0.056	0.040	
g^{eff} [d]	(1.99,1.99,1.98)		(2.41,1.92,1.69)		(1.97,1.97,1.97)		(1.98,1.98,1.98)		(2.00,2.00,1.98)		(1.98,1.94,1.91)
$A_x^{tot}/g_N\beta_N$, T	−27	4.5	−26	5.0	−28	6.2	−29	7.4	−29	8.7	10
$A_y^{tot}/g_N\beta_N$, T	−28	8.4	−20	5.0	−28	6.2	−29	7.4	−29	5.9	10
$A_x^{tot}/g_N\beta_N$, T	−18	1.0	−16	5.0	−28	6.2	−29	0	−15	1.4	14
$A_{iso}^{tot}/g_N\beta_N$, T	24	4.6	−20.7	5.0	−28	6.2	−29	4.9	−24.3	5.3	11.3
$A_x/g_N\beta_N$, T [h]	−19.2	−11.3	−11.1	−3.75	−20.0	−15.5	−20.7	−18.5	−20.7	−21.8	−15.0
$A_y/g_N\beta_N$, T [h]	−20.0	−21	−8.6	−3.75	−20.0	−15.5	−20.7	−18.5	−20.7	−14.8	−15.0
$A_z/g_N\beta_N$, T [h]	−12.9	−2.5	−6.9	−3.75	−20.0	−15.5	−20.7	0	−10.7	−13.3	−21
δ, mm s^{-1} [e]	0.36	0.05	0.38	−0.10	0.44	0.026	0.45	0.00	0.45	0.03	−0.00
ΔE_Q, mm s^{-1} [f]	−0.49	1.14	−0.85	0.86	−0.57	1.74	−0.48	1.07	−0.50	1.67	1.21
η [g]	0.23	0.25	−0.40	0.02	0.04	0.22	0.17	0.97	0.10	0.02	0.02

[a] Ground state. [b] Zero-field splitting parameter. [c] Rhombicity. [d] Electronic g-values for the S = 3/2, M_S = +−1/2 Kramers doublet; or g values of the S = 1/2 state for **1**ox(2nd subspectrum) and **5**ox. [e] Isomer shift vs α-Fe at 80 K. [f] Quadrupole splitting. [g] Asymmetry parameter. [h] Components of the local magnetic hyperfine coupling tensor given with respect to S = 1 (Fe^{IV}) or S = 2 (Fe^{IV}), and S = 5/2 (Fe^{III}).
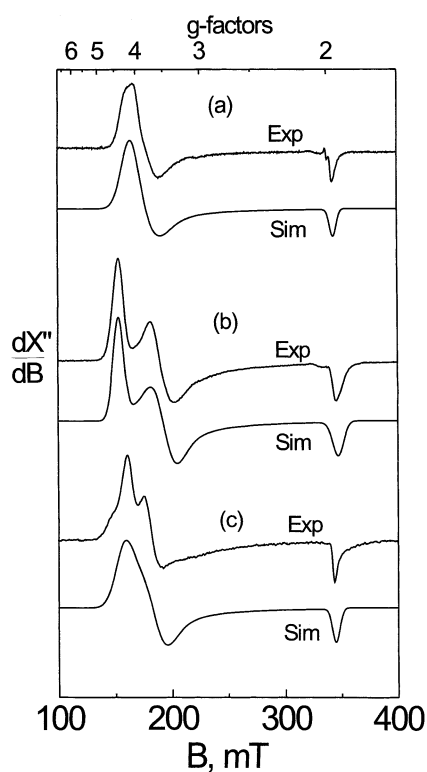

Figure 4. X-Band EPR spectra of electrogenerated **2**ox (a), **3**ox (b), and **4**ox (c) in frozen acetonitrile solution (0.10 M [TBA]PF$_6$). Experimental conditions: (a) temperature: 10 K; microwave frequency: 9.45 GHz, modulation amplitude: 10 G; power: 51 μW; (b) 2.7 K; 9.45 GHz; 10 G; 101 μW; (c) 2.2 K; 9.47 GHz; 12 G; 101 μW. See text for the details of the simulations.

Figure 5. X-Band EPR spectrum of electrogenerated **5**ox in frozen CH$_3$-CN (0.10 M [TBA]PF$_6$) at 10 K. Experimental conditions: microwave frequency: 9.46 GHz, modulation amplitude: 10 G; power: 101 μW. See text for details of the simulation.

spin Fe^{IV}). Antiferromagnetic coupling of either of the two to a high spin ferric (S_{Fe} = $^5/_2$) ion yields the observed ground states of S_t = $^3/_2$ and $^1/_2$, respectively, for **1**ox. This interpretation is consistent with the Mössbauer results. It is, however, in conflict with the EPR measurements on the S = $^1/_2$ species. The large observed positive and negative g-shifts are difficult to reconcile with the presence of a high-spin d^4 (S = 2) species for which, in analogy to the case of high-spin Mn(III), only negative g-shifts are expected. On the other hand, the presence of low spin Fe(III) on the ferric site of the dimer, which would explain the unusual observed g-values, appears to be excluded
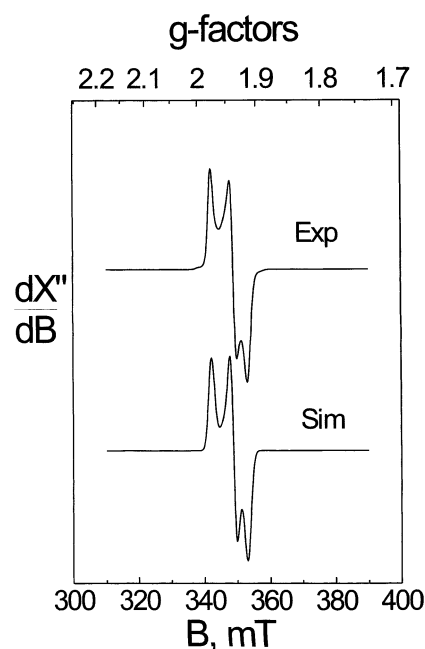
by the Mössbauer results. The real nature of the S = $^1/_2$ species therefore remains elusive at the present stage of investigation.

Mössbauer Spectroscopy. The Mössbauer parameters, namely isomer shift δ and quadrupole splitting ΔE_Q, for the starting materials **2**, **3**, and **5** have been reported previously; the data are summarized in Table 3. We have recorded the zero-field Mössbauer spectra of solid **1** and of the two isotopomers **4a**, **4b**, which all consist of a single quadrupole doublet. The isomer shift for the differing LFe^{III}O$_3$ moieties are observed in the narrow range 0.44−0.52 mm s^{-1}, whereas the relatively large quadrupole splitting $|\Delta E_Q|$ is in the range 1.5−2.0 mm s^{-1}. As shown in Figure 7, by using the isotopomers **4a** and **4b**, it is possible to unambiguously assign the isomer shifts to the two different ferric ions. The (tpb)Fe^{III} fragment displays an isomer shift of 0.52 mm s^{-1} in **3** and **4**, whereas the (Me$_3$[9]aneN$_3$)-Fe^{III} fragment has a slightly smaller value at 0.47 mm s^{-1} in **2**
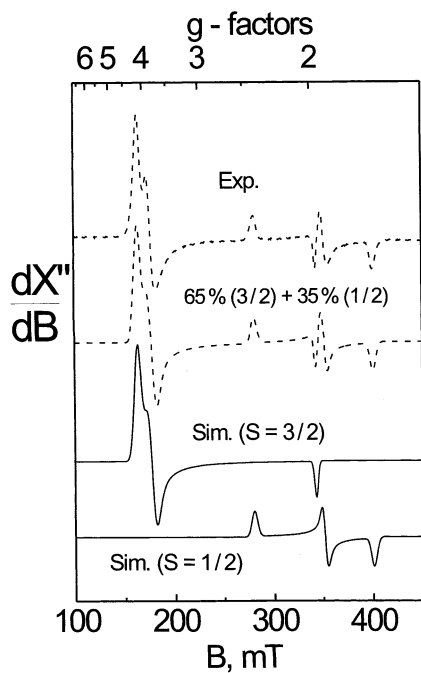
Figure 6. X-Band EPR spectrum of electrogenerated 1^{ox} in frozen CH_3-CN at 10 K. Conditions: microwave frequency: 9.45 GHz, modulation amplitude: 10 G; power: 253 μW. See text for details of the simulation.
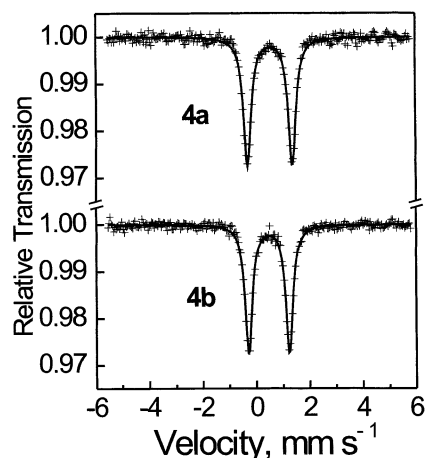

Figure 7. Zero-field Mössbauer spectra of **4a** (top) ((Me_3[9]aneN$_3$)^{57}Fe site labeled with ^{57}Fe) and **4b** (bottom) ((tpb)^{57}Fe site labeled) in frozen CH_3CN solution (0.10 M [TBA]PF$_6$) at 80 K.

and **4** and the ([9]aneN$_3$)Fe unit has an isomer shift of 0.46 in **1** at 80 K.

Upon one-electron oxidation of **5** the isomer shift of the ferric ion *decreases* by 0.54 mm s^{-1} indicating that this process involves the oxidation of the ferric ion affording a low spin Fe^{IV} ion ($\delta = -0.002$ mm s^{-1}, $|\Delta E_Q| = 1.215$ mm s^{-1}) in 5^{ox}. The applied-field Mössbauer spectra of 5^{ox} recorded at 4.2 K are shown in Figure 8 and the parameters derived from simulations are summarized in Table 7. The isotropic part of the A tensor, $A_{iso}/g_N\beta_N = +11.3$ T ($= 1/3$ tr($\mathbf{A}^{tot}$)) is positive, in contrast to the negative value expected for the local contribution from the intrinsic fermi-contact field. This behavior clearly identifies the local spin on the iron center as antiparallel with respect to the total spin $S_t = {}^1/_2$ of 5^{ox}. Thus, the spin coupling scheme is that of Cr^{III}, ($S_{Cr} = 3/2$, majority spin and Fe^{IV}, $S_{Fe} = 1$, minority spin. Note that this result discards the alternative description of the electronic structure of 5^{ox} as that
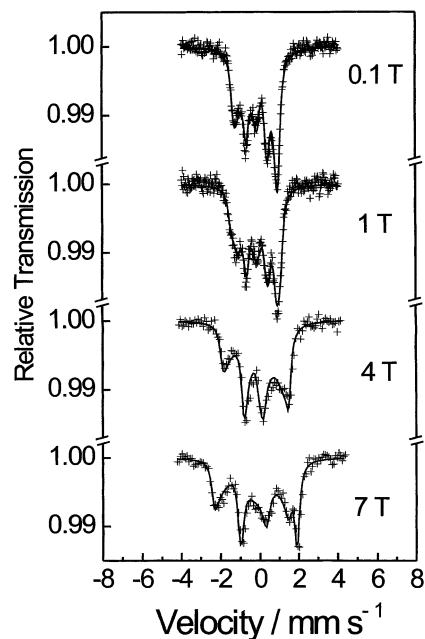
Figure 8. Magnetically perturbed Mössbauer spectra of ^{57}Fe labeled 5^{ox} in frozen CH_3CN solution (0.10 M [TBA]PF$_6$) at 4.2 K. The solid lines represent best fits from the spin-Hamiltonian simulation with $S_t = {}^1/_2$ for a single Fe(IV) ($S_{Fe} = 1$) ion. For parameters see text.

of an antiferromagnetically coupled high-spin Fe^{IV} ion ($S_{Fe} = 2$) and a Cr^{III} ion ($S_{Cr} = {}^3/_2$). From the applied field spectra of **5** ($S_t = 1$) the following parameters have been established:[15] $D^{tot} = +3.9$ cm^{-1}, $E^{tot} = +1.7$ cm^{-1}, $^1/_3$Tr $\mathbf{g}^{tot} = 2.01$, $\mathbf{A}^{tot}/g_N\beta_N = -(33.8, 30.9, 35.8)$ T, ($\mathbf{A}^{Fe}/g_N\beta_N = -(19.3, 17.7, 20.5)$ T; $\mathbf{A}^{Fe} = 4/7$ $\mathbf{A}^{tot}$), $\delta = 0.52$ mm/s, $\Delta E_Q = -2.00$ mm/s, $\eta = 0.22$. The values for $\mathbf{A}^{Fe}$ and ΔE_Q are typical for an octahedral high spin ferric ion. The zfs parameters of the spin triplet of **5** are determined by the properties of the Fe^{III} and Cr^{III} ions according to the relation eq 7 neglecting dipolar

$$D_t = 15/4\ D_{Fe} + 3/10\ D_{Cr} \qquad (7)$$

contributions. Since the zfs of Cr^{III} ions is in general small, $|D_{Cr}| < 1$ cm^{-1},[38] we can estimate $D_{Fe} \approx 4/15\ D_t = 1.4$ cm^{-1} which is typical for octahedral, high spin, non-heme Fe^{III}.[39]

Equation 8 derived for strongly coupled systems according to the Wigner−Eckart theorem allows the calculation of hyperfine coupling constants in the intrinsic representation

$$Fe^{IV}\ (S_1 = 1), Cr^{III}\ (S_2 = {}^3/_2), S_t = {}^1/_2$$

$$\mathbf{A}^{tot}\ (Fe^{IV}) = -{}^2/_3\ \mathbf{A}\ (Fe^{IV}),\ \mathbf{g}_s = -{}^2/_3\ \mathbf{g}_1 + {}^5/_3\ \mathbf{g}_2 \quad (8)$$

This equation allows an interpretation of the observed EPR g values of 5^{ox} $\mathbf{g} = (1.976, 1.938, 1.914)$. A chromium(III) ion

(38) (a) Singer, L. S. *J. Chem. Phys.* **1955**, 23, 379−388. (b) McGarvey, B. R. *J. Chem. Phys.* **1964**, 41, 3743−3758. (c) Pedersen, E.; Toftlund, H. *Inorg. Chem.* **1974**, 13, 1603. (d) Sommerville, D. A.; Jones, R. D.; Hoffman, B. M.; Basolo, F. *J. Am. Chem. Soc.* **1977**, 99, 8195. (e) Bolster, D. E.; Gütlich, P.; Hatfield, W. E.; Kremer, S.; Müller, E. W.; Wieghardt, K. *Inorg. Chem.* **1983**, 22, 1725−1729. (f) Burdinski, D.; Bill, E.; Birkelbach, F.; Wieghardt, K.; Chaudhuri, P. *Inorg. Chem.* **2001**, 40, 1160−1166. (g) Weyhermüller, T.; Paine, T. K.; Bothe, E.; Bill, E.; Chaudhuri, P. *Inorg. Chim. Acta* **2002**, 337, 344−356.
(39) (a) Palmer, G. In *Physical Methods in Bioinorganic Chemistry*; Que, L., Ed.; University Science Books: Sausalito, 2000, pp 121−186. (b) Trautwein, A. X.; Bill, E.; Bominaar, E. L.; Winkler, H. *Struct. Bond.* **1991**, 78, 1−95.
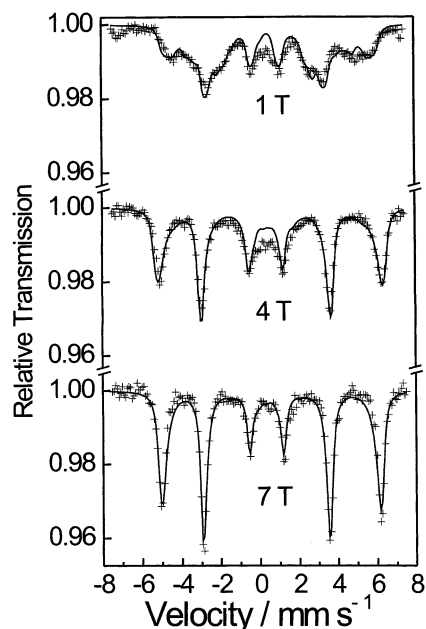
Figure 9. Magnetically perturbed Mössbauer spectra of **4a**^{ox} (^{57}Fe labeled (tpb)Fe^{III} site) in frozen CH$_3$CN solution (0.10 M [TBA]PF$_6$) at 4.2 K. The solid lines represent best fits from the spin-Hamiltonian simulation with S$_t$ = ^{3}/$_2$ for a single Fe^{III} ion (S$_{Fe}$ = ^{5}/$_2$).

even in a quite distorted octahedral ligand field possesses a nearly isotropic intrinsic **g** matrix close to the value of the free electron;[38] calculated and experimental g values are of the order 1.96 to 1.98. By using eq 8 one calculates then a mean g-value of 2.09 for the Fe^{IV} center which is in excellent agreement with other Fe^{IV} (S = 1) ions.[40]

The applied field Mössbauer spectra at 4.2 K of the ^{57}Fe enriched one-electron oxidized isotopomers of [(tpb)^{57}Fe^{III}(μ-O)(μ-CH$_3$CO$_2$)$_2$Fe^{III}(Me$_3$[9]aneN$_3$)]$^+$ (**4a**) and [(tpb)Fe^{III}(μ-O)(μ-CH$_3$CO$_2$)$_2$^{57}Fe^{III}(Me$_3$[9]aneN$_3$)]$^+$ (**4b**), namely of complexes [**4a**^{ox}] and [**4b**^{ox}], are shown in Figures 9 and 10, respectively. The parameters are listed in Table 7. From the isomer shift data it is immediately clear that the (tpb)Fe^{III}O$_3$ moiety contains a ferric ion with δ = 0.45 mm/s and ΔE_Q = −0.51 mm/s whereas the iron ion in the (Me$_3$[9]aneN$_3$)Fe^{IV}O$_3$ unit is oxidized (δ = 0.04 mm/s; ΔE_Q = 1.68 mm/s). The differing signs of the **A**^{tot} tensor components which is negative for **4a**^{ox} but positive for **4b**^{ox} are also consistent with strongly antiferromagnetically coupled sites with the local spin aligned parallel and antiparallel relative to the total spin of S$_t$ = ^{3}/$_2$ as is to be expected from eq 9

$$\text{Fe}^{IV} (S_1 = 1), \text{Fe}^{III} (S_2 = {}^5/_2), S_t = {}^3/_2$$

$$\mathbf{A}^{tot}(\text{Fe}^{IV}) = -{}^2/_5 \mathbf{A} (\text{Fe}^{IV})$$

$$\mathbf{A}^{tot} (\text{Fe}^{III}) = {}^7/_5 \mathbf{A} (\text{Fe}^{III}), \mathbf{g}_s = -{}^2/_5 \mathbf{g}_1 + {}^7/_5 \mathbf{g}_2 \quad (9)$$

The applied field spectra of ^{57}Fe enriched, one-electron oxidized forms of [(Me$_3$[9]aneN$_3$)$_2$^{57}Fe^{III}$_2$(μ-O)(μ-CH$_3$CO$_2$)$_2$]$^{2+}$ and [(tpb)$_2$^{57}Fe^{III}$_2$(μ-O)(μ-CH$_3$CO$_2$)$_2$]^0, namely **2**^{ox} and **3**^{ox}, are shown in Figures 11 and 12, respectively; they both display more complicated patterns resulting from a superposition of the
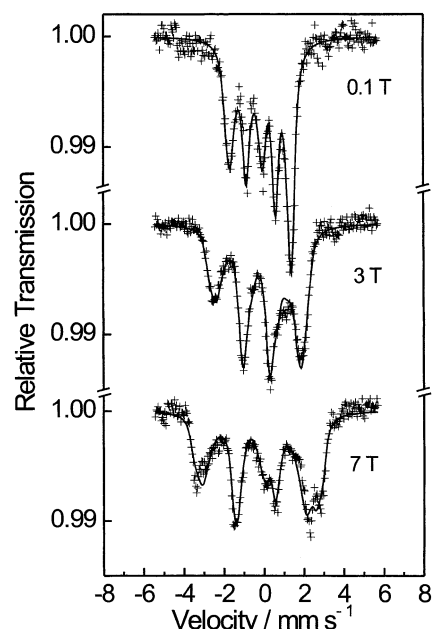
(40) Rohde, J.-U.; In, J.-H.; Lim, M. H.; Brennessel, W. W.; Bukowski, M. R.; Stubna, A.; Münck, E.; Nam, W.; Que, Jr., L. *Science* **2003**, *299*, 1037.

Figure 10. Magnetically perturbed Mössbauer spectra of **4b**^{ox} (^{57}Fe labeled (Me$_3$[9]aneN$_3$)Fe^{IV} site) in frozen CH$_3$CN solution (0.10 M [TBA]PF$_6$) at 4.2 K. The solid lines represent best fits from the spin-Hamiltonian simulation with S$_t$ = ^{3}/$_2$ for a single Fe(IV) (S$_{Fe}$ = 1) ion.
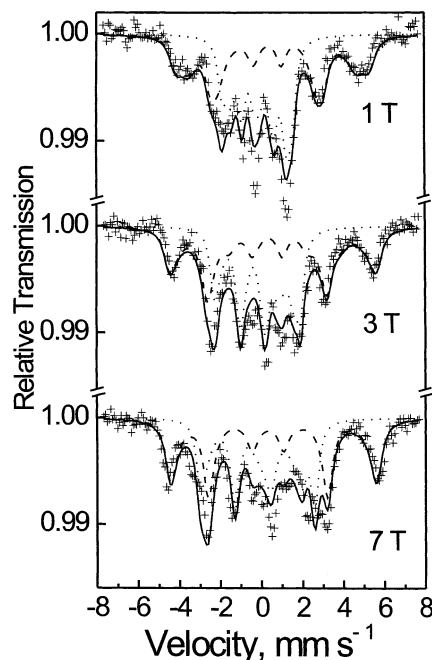

Figure 11. Magnetically perturbed Mössbauer spectra of ^{57}Fe labeled **2**^{ox} in frozen CH$_3$CN solution (0.10 M [TBA]PF$_6$) at 4.2 K. The solid lines represent best fits from the spin-Hamiltonian simulation with S$_t$ = ^{3}/$_2$ and an Fe(IV) (S$_{Fe}$ = 1) ion (dotted line) and an Fe(III) ion (S$_{Fe}$ = ^{5}/$_2$ (dashed line) (ratio 1:1).

signals arising from two inequivalent iron sites, respectively, namely an Fe^{III} and an Fe^{IV} site. It has been possible in both cases to successfully simulate the field dependence of the two subspectra with the assumption of an antiferromagnetically coupled Fe^{IV} (S$_{Fe}$ = 1) and a high spin Fe^{III} (S$_{Fe}$ = ^{5}/$_2$) yielding the S$_t$ = ^{3}/$_2$ ground state. The results of the simulations are given in Table 7.

The Mössbauer spectra of **1**^{ox} shown in Figure 13 were fitted by using two different assumptions for the identity of the
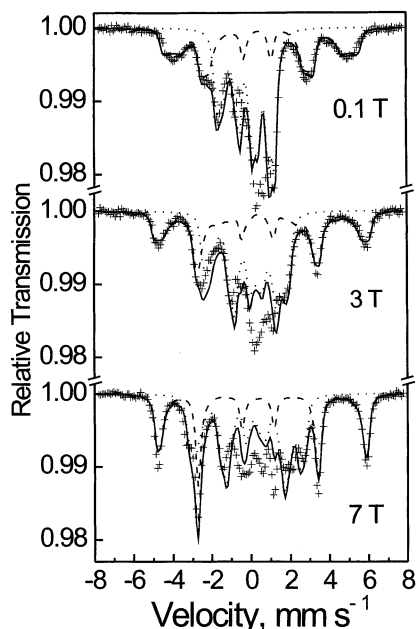
Figure 12. Magnetically perturbed Mössbauer spectra of electrogenerated, [57]Fe enriched **3**[ox] in frozen CH_3CN solution (0.10 M [TBA]PF_6) at 4.2 K. The solid lines represent best fits from a spin-Hamiltonian simulation with $S_t = {}^3/_2$ and an Fe(IV) ($S_{Fe} = 1$) (dotted line) and an Fe(III) ($S_{Fe} = {}^5/_2$) ion (dashed line).
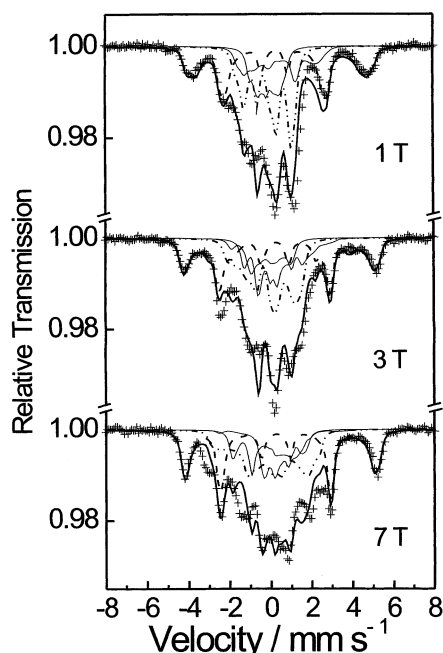

Figure 13. Magnetically perturbed Mössbauer spectra of electrogenerated [57]Fe labeled **1**[ox] in frozen CH_3CN (0.10 M [TBA]PF_6) at 4.2 K. The solid lines represent the results of the simulation based on 65% of an $S_t = {}^3/_2$ species (Fe(IV) dotted line and Fe(III) dashed line) and 35% of an $S_t = {}^1/_2$ species (light solid line) ((Fe(IV) ($S_{Fe} = 2$) and Fe(III) ($S_{Fe} = {}^5/_2$)).

minority $S_t = {}^1/_2$ species: (a) antiferromagnetically coupled Fe-(III) $S = {}^5/_2$ and Fe(IV) $S = 2$; (b) antiferromagnetically coupled Fe(III) $S = {}^1/_2$ and Fe(IV) $S = 1$.

For both situations we employed a common set of spin-Hamiltonian parameters for the majority $S_t = {}^3/_2$ species. For the minority species the A-tensor was constrained to be isotropic.

The quality of the simulations is comparable for both situations. Both assumptions lead to the appropriate signs of the A-tensors in the coupled representation for the $S_t = {}^1/_2$
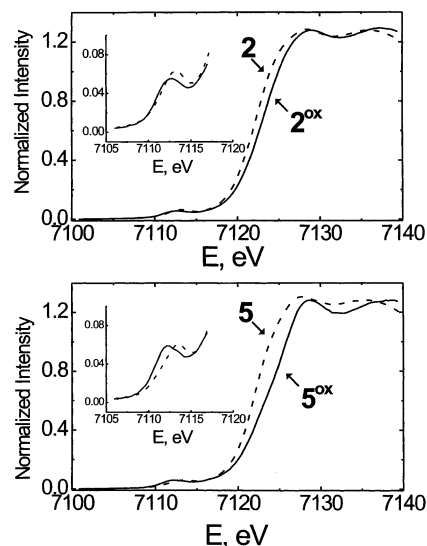

Figure 14. Top: normalized XANES spectra of **5** and electrogenerated **5**[ox] in electrochemically CH_3CN solution (dashed and solid lines, respectively) at 20 K. Bottom: normalized XANES spectra of **2** and **2**[ox] (dashed and solid lines, respectively). The insets show the preedge-peaks (1s → 3d transitions) of these species.

species, but the intrinsic A values for the Fe(III) site in (a) and for the Fe(IV) site in (b) deviate from what is expected for an Fe(III) ($S = {}^5/_2$) and an Fe(IV) ($S = 1$), respectively. This is essentially a consequence of the fact that the $S_t = {}^1/_2$ component contributes to only 35% of the total intensity, which correlates perfectly with the composition of the EPR spectrum. The fact that this species presents features only in the crowded inner region of the spectrum makes it difficult, if not impossible, to estimate the reliability of the fitting parameters. On the basis of these results, we understand that we cannot discern between both possibilities by Mössbauer spectroscopy. Nevertheless, the line pattern arising from the $S_t = {}^3/_2$ is reproduced nicely in both simulations, particularly the outermost lines originated in the Fe(III) ($S = {}^5/_2$) site. This suggests that the spin-Hamiltonian parameters derived for this latter species are correct. The obtained parameters collected in Table 7 compare well with the values observed for the other oxidized species.

XANES Spectroscopy. The X-ray absorption near edge spectra (XANES) of **2**, **4**, **5** and of their electrochemically generated oxidized forms **2**[ox] and **5**[ox] have been recorded at the Fe K edge. XAS as an element specific spectroscopy allows to analyze the oxidation state of a given element in a coordination compound. The position and intensity of the resonances and, in particular, the energy of the absorption edge position are features which depend on the electronic configuration. We have determined the edge positions from the maximum of the first derivative of the data in the rising edge region. The Fe K edge spectra of **2**, **2**[ox], and **5**, **5**[ox] are shown in Figure 14 and the energies of the edge positions are summarized in Table 2.

The most salient feature is the observation that the energy of the Fe−K edge position shifts to significantly higher values on going from **5** to **5**[ox] both of which compounds contain a single iron ion per dinuclear unit. On going from **2** to **2**[ox], the energy still shifts to higher energies but only approximately half as much. Thus, one iron(III) ion has been oxidized to an Fe[IV] ion in both **2**[ox] and **5**[ox]. In **2** and **5** containing high spin ferric ions the feature at 7136 eV has a larger intensity than the peak at 7128 eV as is expected for six-coordinate ferric complexes with

Table 8. Structural Data Obtained from EXAFS Analyses

complex	ligands	R, Å ^{a}	σ^2_i, Å$^{2\,b}$	EF, eV ^{c}	FI × 10$^{-4\,d}$	F-test ^{e}
2	1Fe	3.120(8)	0.0045(6)	−3.8(4)	3.03	0.89
	1O	1.802(7)	0.0044(7)			
	2O	2.034(5)				
	2N	2.198(6)				
	1N	2.272(13)				
	11C	3.040(10)				
	2O	3.422(36)				
2^{ox}	1Fe	3.173(6)	0.0045(11)	−2.8(4)	2.83	0.91
	0.5O	1.725(15)	0.0045(13)			
	2O	1.934(4)	0.0045(13)			
	1.5N	2.069(19)				
	0.5N	2.270(44)				
	11C	2.936(19)	0.0157(9)			
	2O	3.418(36)				
5	1Cr	3.126(10)	0.0019(5)	−3.8(4)	3.65	0.96
	1O	1.805(5)	0.0015(5)			
	2O	2.049(4)				
	3N	2.199(4)				
	8C	2.948(12)				
	2O	3.229(42)				
5^{ox}	1Cr	3.200(11)	0.0043(11)	−2.8(5)	3.10	0.68
	1O	1.692(8)	0.0045(15)			
	2O	1.930(30)				
	3N	2.004(24)				
	8C	2.880(13)				
	2O	3.293(53)				

^{a} Distance between iron and backscattering atom; in brackets the 2σ error levels are given. ^{b} Debye−Waller factor comprising statistical and dynamical disorder. ^{c} Fermi energy. ^{d} Fit index. ^{e} Statistical probability for the presence of the second metal atom.

a μ-oxo bridge whose short Fe−O$_{oxo}$ bonds enforce a strong mixing of the $3d_{z^2}$ and $4p_z$ orbitals. For the oxidized species **2^{ox}**, **5^{ox}** the pre-edge features are shifted to lower energies with a smaller peak at low energy and a broader one at higher energy.

EXAFS Spectroscopy. Analyses of the EXAFS spectra of complexes **2** and **5** containing ferric ions are in excellent agreement with the structural data obtained from single-crystal X-ray crystallography. Table 8 gives the results of the EXAFS analyses which may be compared with known crystallographic data compiled in Table 3.

The data for **5^{ox}** are interesting because only a single iron ion in the oxidation state +IV (S$_{Fe}$ = 1) is present. The structural differences between **5** and **5^{ox}** are therefore representative for all one-electron oxidations in the present series. Thus, the Fe−O$_{oxo}$ distance decreases from 1.805(5) in **5** to 1.692(8) Å in **5^{ox}** (Δ = 0.113 Å) and, similarly, the Fe−N distances are shorter by 0.195 Å and the Fe−O$_{carboxylato}$ bonds are also shorter by 0.12 Å in **5^{ox}** as compared to **5**. Similar bond length differences are observed on going from **2** to **2^{ox}**. It is noted that the Fe−O−Fe bridge in **2^{ox}** is asymmetric with a short Fe^{IV}−O$_{oxo}$ bond at 1.725(15) Å and a long Fe^{III}−O$_{oxo}$ bond at ~1.94 Å since the best fit index was found for a single short Fe−O$_{oxo}$ distance (occupation 0.5). Recently, the crystal structure of a six-coordinate mononuclear Fe(IV)=O with an S = 1 ground state has been reported.[40] The Fe=O$_{terminal}$ bond distance at 1.646-(3) Å is, as expected, slightly shorter than the Fe^{IV}=O$_{bridge}$ bond in the present dinuclear complexes.

Table 9. Predicted Structural, Magnetic and Mössbauer Spectral Parameters from DFT Calculations as Described in the Text

complex	4	4^{ox}	5	5^{ox}
Fe−O$_{oxo}$, Å	1.90, 1.84^e	2.15, 1.69^e	1.82	1.72
Fe−O$_{carboxylato}$, Å	2.12, 2.04	2.06, 1.93	2.07	1.93
Fe−N, Å	2.15, 2.33	2.12, 2.12	2.27	2.06
Cr−O$_{oxo}$, Å			1.92	1.99
Cr−O$_{carboxylato}$, Å			2.00	1.98
Cr−N, Å			2.18	2.15
J, cm$^{-1\,a}$	−79	−57	−82	−81
δ, mm/s^b	Fe$_A$:0.50 Fe$_B$:0.50^e	Fe$_A$:0.50 Fe$_B$:0.10^e	Fe:0.47	Fe:0.05
ΔE_Q, mm/s^c	Fe$_A$:−1.34 Fe$_B$:−1.49	Fe$_A$:0.24 Fe$_B$:1.48	Fe:−1.90	Fe:1.69
η^d	Fe$_A$:0.07 Fe$_B$:0.19	Fe$_A$:0.22 Fe$_B$:0.20	Fe:0.05	Fe:0.23

^{a} Exchange coupling constant; ($H = -2J$ S$_A$·S$_B$). ^{b} Isomer shift. ^{c} Quadrupole splitting. ^{d} Asymmetry parameter. ^{e} The first number refers to (tpb)Fe site and second to the (Me$_3$[9]aneN$_3$)Fe site.

Very similar bond length differences between equivalent Fe-X bonds of high spin ferric and of the corresponding Fe^{IV} (S$_{Fe}$ = 1) part of the following dinuclear, crystallographically characterized complex [(Me$_3$[9]aneN$_3$)(Ph$_2$acac)Fe^{III}(μ-N)Fe^{IV}(Cl$_4$-cat)-(Me$_3$[9]aneN$_3$)](ClO$_4$) have been observed.[41] It is also very gratifying that for all complexes, irrespective of the oxidation level, an Fe···metal vector at ~3.2 Å has been unequivocally identified. This distance *increases* only slightly (~0.06 Å) on going from **2**, **5** to their oxidized counterparts **2^{ox}** and **5^{ox}**. This proves that the (μ-oxo)bis(μ-carboxylato)dimetal core is retained in **2^{ox}** and **5^{ox}** since the di(μ-carboxylato)dimetal core gives rise to metal···metal distances of ~4.2 Å.[42] Figures S3, S4 show the best fits of the Fourier transforms of the EXAFS data for complexes **2**, **2^{ox}**, **5** and **5^{ox}**.

Calculations. 1. Structure Optimizations. Density functional theoretical calculations have been carried out at the BP86 and B3LYP levels for complexes **4** and **5** and their one-electron oxidized counterparts **4^{ox}** and **5^{ox}**. Table 9 summarizes the calculated bond lengths for these species which are based on the high-spin calculations (spin unrestricted calculation with M$_S$ = S$_a$ + S$_b$ where S$_a$ and S$_b$ are the hypothetical site spins).

The agreement between the experimental and calculated structural parameters for the dinuclear complexes **4** and **5** is reasonably good. The geometrical details of the Fe−O−M cores and, in general, all features of the {Fe^{III}(μ-O)(μ-acetato)$_2$M^{III}}$^{2+}$ cores in **4** and **5** are correctly reproduced. The DFT calculations at the BP86 level tend to slightly overestimate the bond lengths for weak metal−ligand bonds and average deviations of ~0.05 Å are usually observed. Here the differences appear to be slightly larger. The optimized structure of **5^{ox}** clearly shows that it is the iron ion in **5** which is oxidized to an Fe(IV) ion. All six Fe−X bonds in **5^{ox}** are shorter than those in **5**. The Fe−O−Cr moiety in **5^{ox}** is more asymmetric than in **5** due to a shorter Fe−O$_{oxo}$ bond and a longer Cr−O$_{oxo}$ bond (Table 9). The quantitative agreement between the calculated structure of **5^{ox}** and the EXAFS experiments is encouraging and validates our theoretical approach. Similar conclusions can be drawn from the calculation of the structure of **4^{ox}**. It is the (Me$_3$[9]aneN$_3$)-Fe site which is oxidized because here the six Fe−X bonds contract in comparison with **4**, whereas those of the (tpb)Fe moiety remain essentially the same in both **4** and **4^{ox}**.

(41) Jüstel, T.; Müller, M.; Weyhermüller, T.; Kressl, C.; Bill, E.; Hildebrandt, P.; Lengen, M.; Grodzicki, M.; Trautwein, A. X.; Nuber, B.; Wieghardt, K. *Chem. Eur. J.* **1999**, *5*, 793.
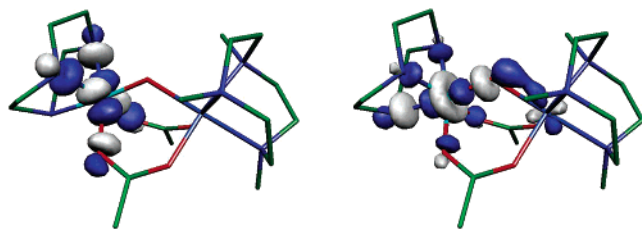(42) Lee, D.; Lippard, S. J. *J. Am. Chem. Soc.* **1998**, *120*, 12 153.

Figure 15. Two MOs on the iron site of **5** that become depopulated in **5**^{ox} obtained from BS-B3LYP calculation on **5**^{ox}. Left: the Fe-d_{x2-y2} based MO, right: the Fe-d_{z2} based MO.

2. Mössbauer Parameters. The calculations can be further put to a critical test by calculating the isomer shift and quadrupole splitting at the iron sites. Both quantities are local properties of the iron ions and react sensitively to any qualitative and to a certain extent also quantitative errors in the calculated electronic structure. In general, the agreement between the experimental (Table 7) and calculated (Table 9) parameters is good. The predicted δ values for **4**, **4**^{ox} and **5**, **5**^{ox}, based on the computation of the electron density at the Fe nucleus provides particularly accurate results.[34] The computed ΔE_Q values are in good quantitative agreement for **5** and **5**^{ox}, clearly reflecting the changes observed experimentally upon oxidation. The trend in the ΔE_Q values is interpreted as follows: in the homovalent Fe(III)/Fe(III) case the octahedron is rather strongly distorted electronically due to the strong Fe(III)−oxo bond. Consequently, one observes a rather large quadrupole splitting (a perfect octahedral site would give $\Delta E_Q = 0$). In the heterovalent case, the Fe(IV)−oxo bond becomes stronger and shorter, whereas the Fe(III)−oxo bond becomes weaker and longer. Consequently, for the Fe(III) site the environment approaches more closely that of a regular octahedron and the ^{57}Fe quadrupole splitting is expected, observed, and calculated to strongly decrease. The calculated ΔE_Q value for **4**^{ox} is a little disappointing, particularly on the Fe(III) site where the quadrupole splitting is small and the calculations predict the wrong sign. A plausible explanation for this result is that the calculations are underestimating the degree of covalency of the Fe(III)−O, thus leading to a too symmetric electron density around the Fe(III) which in turn suggests that we are probably overestimating the Fe(III)−O bond length. This does not affect the calculated g-values because of the essentially isotropic nature of the Fe-(III) site even in distorted octahedral environments, but is not clear to us why the isomer shift remains within reasonable values. In any case, all computational results indicate that the structural characteristics of the Fe(IV) site and their impact on its electronic properties are well taken into account.

3. Electronic Structure. The structural changes that occur upon oxidation of **4** and **5** can be traced back to the changes in the orbital configurations for both species. Both **4** and **5** feature a high-spin ferric ion with all five Fe-3d based MOs being singly occupied by electrons with the same spin. Upon oxidation to the Fe(IV) state the two Fe-3d based MOs with e_g parentage in octahedral symmetry become depopulated as can be seen from the contour plots of the two spin-down LUMOs of the BS-B3LYP calculation on **5**^{ox} (Figure 15). One of the two e_g electrons is lost in the oxidation, whereas the other one flips spin and pairs with the electron which occupied the iron-d_{xy} based MO as will become evident in the inspection of the magnetic orbitals of **5**^{ox} in the next section. Because the two most antibonding interactions between the iron site and the

Table 10. Calculated Löwdin Charges, Löwdin Spin Densities and Wiberg Bond Indices for **4**, **4**^{ox}, **5**, and **5**^{ox} from BS-B3LYP Calculations^a

complex	4	4^{ox}	5	5^{ox}
charge-Fe	0.642	0.316	0.653	0.363
charge-X	0.759	0.795	0.305	0.331
charge-oxo	−0.577	0.400	−0.517	−0.358
spin-Fe	4.102	−1.343	4.118	−1.693
spin-X	−4.202	4.251	−2.937	3.017
spin-oxo	0.108	−0.464	0.351	0.436
Fe-X bond order	0.099	0.066	0.094	0.084
Fe-oxo bond order	0.983	1.435	0.987	1.296
X-oxo bond order	0.838	0.425	0.979	0.744

^{a} X = Fe in **4**,**4**^{ox} and Cr in **5**,**5**^{ox}.

ligands are lost, all metal−ligand distances shrink considerably as a result of the oxidation and become stronger. This is also directly reflected in the calculated electron and spin populations and Wiberg Bond indices which are collected in Table 10. In particular, the iron-oxo bonds becomes much stronger upon oxidation due to the loss of the strongly antibonding σ-interaction between the iron d_{z2} and oxo-p_z orbitals. At the same time, the oxo ligand becomes a better donor to the Fe(IV) site which explains the charge flow from the oxo-ion to the iron which is clearly seen in Table 10.[43] The S = 1 configuration on the Fe-(IV) ion is also clearly inferred from this Table. The values for the Löwdin spin populations are reduced from the ionic limit (spin population = −2.0 in the BS state) to values between −1.0 and −2.0. Consequently, the bridge also becomes asymmetric which is consistent with the calculated geometries and EXAFS results. The spectator metal (Cr(III) in **5** and Fe(III) in **4**) become slightly more positive upon oxidation of the complexes which is explained by an overall increased electron affinity of the Fe(IV) site. Interestingly, the calculated Löwdin charges on the iron site do not reflect the oxidation process at all. The loss of charge from the iron site appears to be more than compensated by the strongly increased covalent interactions with the ligands.

4. Exchange Coupling. Experimentally, it is well established that in complexes containing two high-spin ferric ions connected by a bent μ_2-oxo bridge the spins couple in an antiferromagnetic fashion ($J \approx -120$ cm^{-1}, H = $-2J$ S$_1$·S$_2$, S$_1$ = S$_2$ = $^5/_2$) yielding an $S_t = 0$ ground state. On the basis of eq 9, we have calculated the exchange coupling constants, J, for complexes **4** and **5** and their oxidized forms **4**^{ox} and **5**^{ox} from BS−B3LYP calculations using Yamaguchi's equation[44] (Table 9)

$$J = -\frac{E_{HS} - E_{BS}}{\langle \hat{S}^2 \rangle_{HS} - \langle \hat{S}^2 \rangle_{BS}} \quad (10)$$

For **4** and **5**, the calculated values for J are smaller than the experimental ones. This is partially due to the selection of the

(43) It is commonly observed that the calculated Löwdin charges do not reflect the oxidation or reduction events with nearly integer changes in the calculated charges. This is partly due to the large electronic relaxation effects accompanying ionization events and also to the problem of properly dividing the charge in the bond region and the 4s population between the metal and ligand atoms. The 4s orbital has a probability density maximum roughly at the position of the ligands. Assigning its contribution to the iron is therefore problematic. The spin densities on the other hand are dominated by the compact 3d shell and reflect the actual events more closely. Due to these difficulties one should not equate the changes in Löwdin charges with shifts in edge energies. A proper calculation of edge energies and preedge intensities is beyond the scope of this paper.
(44) Yamaguchi, K.; Takahara, Y.; Fueno, T. In. *Applied Quantum Chemistry*; Smith, V. H., Ed.; Reidel: Dordrecht, 1986; p 155.
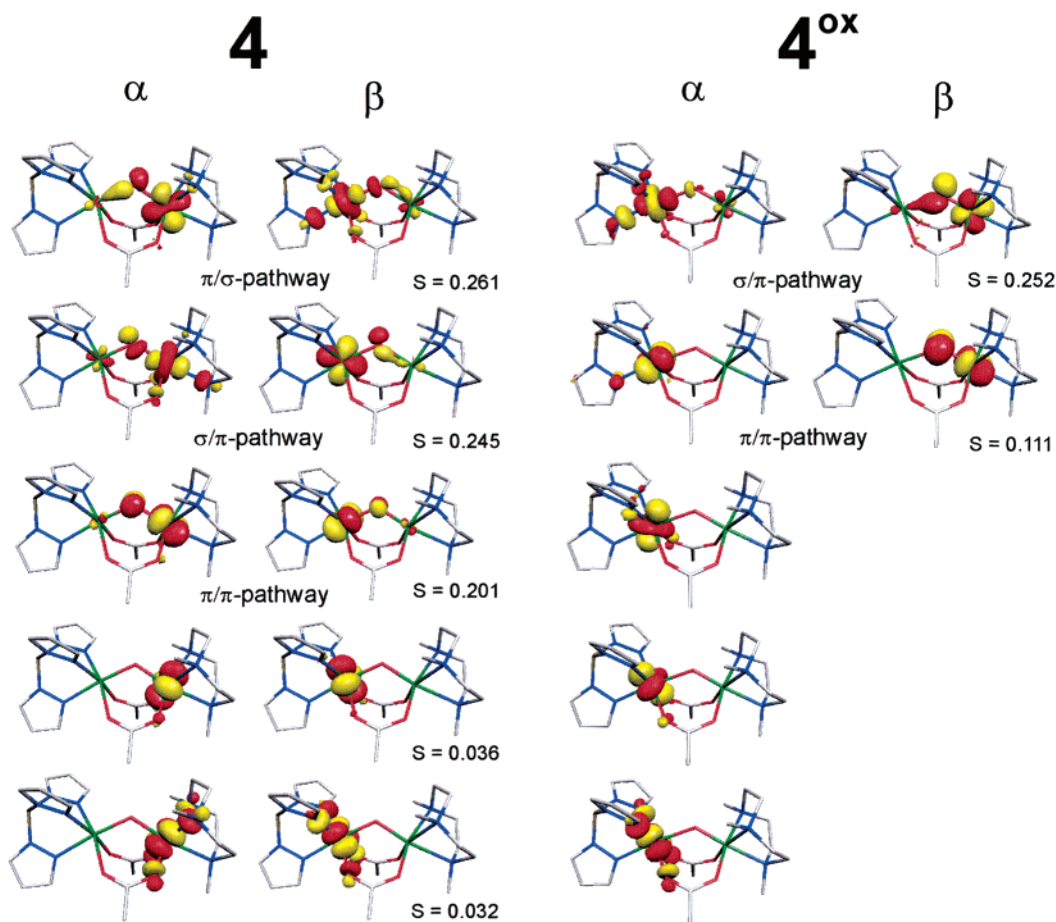
Figure 16. Magnetic orbitals for compounds **4** and **4**^ox at the BS-B3LYP level of theory, as obtained from the corresponding orbital transformation (see text). Note that there is a (tpb)Fe^III *and* a (Me_3[9]aneN_3)Fe site in **4** and **4**^ox, respectively.

HS geometry for the single point calculations; the HS equilibrium geometry minimizes E_{HS} at the expense of the slightly overestimated E_{BS}. If the calculations are carried out at the BS equilibrium geometry, then the opposite effect is observed (minimum E_{BS}, overestimated E_{HS}) yielding larger calculated values for J. Nevertheless, the agreement between experimental and calculated J values is acceptable, and the differences are within the errors experienced in such calculations.[45]

As we have discussed previously,[37] one can use the corresponding orbital transformation[36] to visualize the overlapping magnetic orbitals pairs of the system. The procedure involves a unitary transformation of the spin−orbitals obtained from a single point unrestricted calculation within each spin manifold in such a fashion that for each spin-up transformed orbital there exists at most one spin-down partner that has nonzero spatial overlap with it. Values of S close to 1 identify the normal unrestricted solutions with some spin polarization, whereas S

values <1 are the signature for nonorthogonal magnetic orbitals of BS magnetic orbital pairs.

The orbitals arising from calculations on the BS states of **4** and **5** are displayed in Figures 16 and 17, respectively. This pictorial representation not only allows us to keep track of the number of unpaired electrons at each metal site but also enables us to visualize the interactions between them. Inspection of these orbitals reveals three important antiferromagnetic exchange pathways in **4** (Figure 16): a π/σ-pathway, a σ/π- and a π/π-interaction in agreement with previous analyses for (μ-oxo)bis (μ-carboxylato)diferric species.[46] In contrast, only two important antiferromagnetic exchange pathways are identified for **5** (Figure 17). Due to the absence of unpaired electrons in σ-orbitals at the Cr(III) site in **5** the π/σ-pathway should serve as a ferromagnetic pathway.[47] However, somewhat surprisingly, both **4** and **5** nevertheless have almost identical predicted J values.

In agreement with experiment, the calculations also indicate that the spins in **4**^ox and **5**^ox couple antiferromagnetically. The respective J values in Table 9 indicate that in the case of **4**^ox, the coupling is weaker than in the reduced form. Analysis of the corresponding magnetic orbitals is at least qualitatively consistent: the strong π/σ-pathway is absent in **4**^ox because the Fe(IV) ion has a low-spin configuration and only features two

(45) Experimental magnetic susceptibility data are adiabatic measurements and the fairest comparison between theory and experiment would therefore involve comparison of fully relaxed structures for all spin states. However, such a geometry dependence is already beyond the scope of the Heisenberg Hamiltonian and would lead to deviations from the regular spin ladder. In addition, there are the technical difficulties of obtaining the geometry of the low-spin state as opposed to the BS state and problems of numerical precision because the energy differences involved are very small. These effects may be ignored if the geometric relaxation effects are very small. However, in the present work, we have observed some uncomfortably large variations of geometry with spin state (HS or BS). Because geometrical parameters are only known for one of the spin states from the EXAFS and X-ray crystallographic experiments, we prefer to estimate the exchange couplings using the standard approach of fixed geometry calculations.

(46) (a) Brown, C. A.; Remar, G. J.; Musselman, R. L.; Solomon, E. I. *Inorg. Chem.* **1995**, *34*, 688 (b) Solomon, E. I. Brunold, T. C.; Davis, M. I.; Kemsely, J. N.; Lee, S.-K., Lehnert, N.; Neese, F.; Skulan, A. J.; Yang, Y.-S., Zhou, J. *Chem. Rev.* **2000**, *100*, 235.
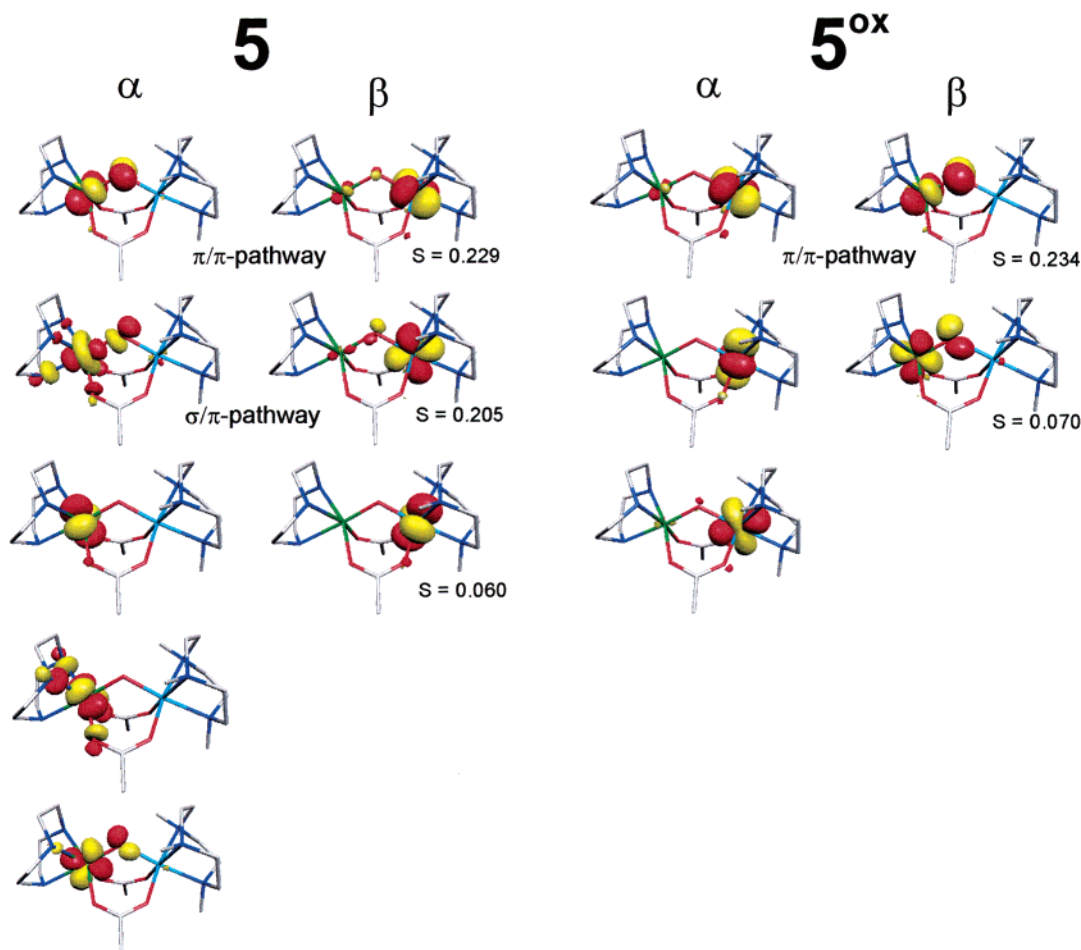(47) Weihe, H.; Güdel, H. U. *Inorg. Chem.* **1997**, *36*, 3632.

Figure 17. Magnetic orbitals for compounds **5** and **5**^{ox} at the BS-B3LYP level of theory, as obtained from the corresponding orbital transformation (see text). Note that there is a (Me₃[9]aneN₃)Cr^{III} and a ([9]aneN₃)Fe site in **5** and **5**^{ox}, respectively.

Table 11. Calculated EPR Parameters Using the BS-B3LYP Approach

	4^{ox}	5	5^{ox}
g$_{tot}$	1.997, 1.999, 2.008 (2.001)	2.018, 2.027, 2.004 (2.026)	1.948, 1.954, 1.974 (1.959)
g(Fe(III)) or **g**(Cr(III))	2.007, 2.009, 2.010 (2.009)	1.985, 1.988, 1.990 (1.988)	1.987, 1.988, 1.990 (1.988)
g(Fe(IV)) or **g**(Fe(III))	2.014, 2.033, 2.034 (2.027)	2.006, 2.011, 2.013 (2.010)	2.014, 2.039, 2.074 (2.033)

ᵃ In brackets g_{iso}.

d_π and no d_σ magnetic orbitals. The π/π-pathway is weaker in **4**^{ox} than in **4**, probably because of the asymmetry of the oxo-bridge which leads to longer Fe^{III}–O$_{oxo}$ bond in **4**^{ox} than in **4**.

By contrast, the J-value for **5**^{ox} is almost identical with that for **5**. This may be traced back to the fact that neither **5** nor **5**^{ox} have a strong antiferromagnetic π/σ-pathway. Thus, the main contribution to J must come from the π/π-pathway which is operative in both, **5** and **5**^{ox}.

In any case, the J values (observed and calculated) are large enough to justify the assumptions made in the analysis of the EPR and Mössbauer spectra. In particular, at the given temperature of these experiments there are no detectable contributions from excited spin multiplets.

5. g-Values. The calculation of the dimer g-tensor for an antiferromagnetically coupled dimer is difficult due to the fact that the BS Kohn–Sham determinant is not an appropriate starting point for a linear response treatment that should be performed with the proper multideterminantal antiferromagnetically coupled state as reference. However, in this section

we will develop a simple approach that lets us arrive at reasonable predictions of g-tensors for antiferromagnetically coupled dimers and which is within the spirit of the BS approach for the calculation of exchange coupling constants.

The main idea involved is to extract the hypothetical site-g-tensors from individual high-spin and BS calculations and then couple the two individual tensors by straightforward vector coupling to give a tensor which appropriately reflects the properties of the antiferromagnetic state. Within the coupled-perturbed Kohn–Sham (CP–KS) theory,[33b] and neglecting the gauge and the relativistic mass corrections, the g-matrix elements for a monomeric (uncoupled) center A can be calculated by means of eq 11, where $\Delta g_{\mu\nu}$ ($\mu, \nu = x, y, z$) describes the departure form the free electron g-value

$$\Delta g_{\mu\nu}^A = \frac{1}{S_A}[\sum_{ia} \Delta_{ia\alpha}^{-1} L_{ia}^{\alpha\mu} \tilde{L}_{ia}^{\alpha\nu} - \sum_{ia} \Delta_{ia\beta}^{-1} L_{ia}^{\beta\mu} \tilde{L}_{ia}^{\beta\nu}] \quad (11)$$

In the above expression, the summation runs over all the

occupied (ψ_i) and empty (ψ_a) orbitals of a given spin $\sigma = \alpha, \beta$, respectively, $\Delta_{ia\sigma} = \epsilon_{a\sigma} - \epsilon_{i\sigma}$ are orbital energy differences, and

$$L_{ia}^{\sigma\mu} = \text{Im}(\langle \psi_i^\sigma | \hat{l}_\mu | \psi_a^\sigma \rangle) \qquad (12)$$

$$\tilde{L}_{ia}^{\sigma\mu} = \text{Im}(\langle \psi_i^\sigma | \sum_A \xi(r_A) \vec{l}_{A,\mu} | \psi_a^\sigma \rangle) \qquad (13)$$

where the operator in eq 12 is the angular momentum operator, and the one in eq 13 is an approximation to the reduced spin−orbit coupling (SOC) operator (for details, see ref 33b). The important point is that the spin-up and spin-down orbital pairs contribute with opposite signs to the computed g-shift and for the sake of the argument eq 11 can be abbreviated as follows

$$\Delta g_{\mu\nu}^A = \frac{1}{S_A}[L^\alpha - L^\beta] \qquad (14)$$

and analogously, for an uncoupled center B, eq 15

$$\Delta g_{\mu\nu}^B = \frac{1}{S_B}[L^{\alpha\prime} - L^{\beta\prime}] \qquad (15)$$

For two coupled centers, A and B, in the high spin and BS limits the g-matrix elements then become eqs 16 and 17

$$\Delta g_{\mu\nu}^{HS} = \frac{1}{(S_A + S_B)}[(L^\alpha - L^\beta) + (L^{\alpha\prime} - L^{\beta\prime})] \qquad (16)$$

$$\Delta g_{\mu\nu}^{BS} = \frac{1}{|S_A - S_B|}[(L^\alpha - L^\beta) - (L^{\alpha\prime} - L^{\beta\prime})] \qquad (17)$$

where the contributions arising from both metal centers were separated which is reasonable if the main contributing orbital pairs are localizable which is an assumption that is at the heart of antiferromagnetic coupling theory.[47] It follows that the HS and BS g-matrix elements are related to the single site g-matrices of centers A and B according to eqs 18 and 19

$$\Delta g_{\mu\nu}^{HS} = \frac{S_A}{S_A + S_B} \Delta g_{\mu\nu}^A + \frac{S_B}{S_A + S_B} \Delta g_{\mu\nu}^B \qquad (18)$$

$$\Delta g_{\mu\nu}^{BS} = \frac{S_A}{|S_A - S_B|} \Delta g_{\mu\nu}^A - \frac{S_B}{|S_A - S_B|} \Delta g_{\mu\nu}^B \qquad (19)$$

Equations 18 and 19 allow the calculation of the hypothetical single site-g-matrices, $g_{\mu\nu}^A$ and $g_{\mu\nu}^B$ which can then be combined to provide the g-tensor for the coupled system in the strong antiferromagnetic coupling limit,[48,49] eq 20

$$\Delta g_{\mu\nu}^{AF} = \frac{S_A + 1}{1 + |S_A - S_B|} \Delta g_{\mu\nu}^A - \frac{S_B}{1 + |S_A - S_B|} \Delta g_{\mu\nu}^B \qquad (20)$$

Using this methodology the g-tensors of $\mathbf{4^{ox}}$, $\mathbf{5}$, and $\mathbf{5^{ox}}$ where

(48) Bencini, A.; Gatteschi, D. *EPR of Exchange Coupled Systems*; Springer: Heidelberg, 1990.

(49) It can be shown that for two exchanged-coupled spins S_A and S_B, the overall g-tensor can be related to the single site **g** and zero-field-splitting **d** tensors by $\mathbf{g} = c_A\mathbf{g}_A + c_B\mathbf{g}_B + c_Ac_B/5J\,(\mathbf{g}_A - \mathbf{g}_B)[(3c_A + 1)\mathbf{d}_A - (3c_A + 1)\mathbf{d}_B]$, where the spin projection factors c_A and c_B can be calculated according to $c_A = S_A(S_A + 1) - S_B(S_B + 1) + S(S + 1)/2S(S + 1)$ and $c_B = S_B(S_B + 1) - S_A(S_A + 1) + S(S + 1)/2S(S + 1)$. In the limit of large $|J|$ only the first two terms contribute to the observed g tensor, and the single-site zfs contribution can be neglected in the prediction of the g-values.

calculated. According to the results in Table 11, **5** posseses an almost isotropic g-tensor, with $g_{iso} = 2.026$. This species is EPR silent, but this number is consistent with the $g = 2.0$ used to analyze the susceptibility and magnetic Moessbauer measurements. The calculated value arises from spin projection of the single-site g-values. It is well-known that the d^5 HS configuration in a pseudo-octahedral environment does not lead to any deviation from the free electron g-values, whereas for the d^3 case in a similar environment all the three principal components of the g-tensor are expected to be below 2.0.[50] On the basis of eqs 14 and 15 we estimate the single-site isotropic contributions as 2.010 and 1.988 for the Fe(III) and Cr(III) sites, respectively. It is rewarding to observe that the g-matrix for $\mathbf{4^{ox}}$ and $\mathbf{5^{ox}}$ is indeed correctly predicted by this simple approach. For the former, we estimate the components of g as [1.997; 1.999; 2.008] ($g_{iso} = 2.001$) in concordance with the EPR results. Furthermore, the calculated $g = $ [1.948; 1.954; 1.974] for $\mathbf{5^{ox}}$ is in excellent agreement with the rhombic signal obtained experimentally. The calculations do underestimate this rhombicity somewhat and give g_{min} and g_{mid} shifts which are too small by ~ 0.02. On the basis of previous experience with DFT g-tensor calculations on transition metal complexes[33b] this result should still be regarded as satisfactory. In both cases, the single site contribution from the Fe(IV) becomes close to 2.03, in good agreement with the expectations (see above the discussion of the X-band EPR spectra). The Fe(IV) g-tensor is not isotropic, a fact which is reflected in $\mathbf{5^{ox}}$ and not in the other $Fe_2^{III,IV}$ species because of the differences in the spin projection factors.

In conclusion, the initial set of calculations reported here corroborates the results of the experimental analysis. Through the successful calculation of the spectroscopic parameters of $\mathbf{4^{ox}}$ and $\mathbf{5^{ox}}$, it is reasonable to claim that the calculated structures of these species are realistic and their electronic structure is indeed described, at least qualitatively, correctly by the DFT methods used.

Conclusion

Although the {Fe^IV(μ-O)(μ-carboxylato)₂Fe^III}^{3+} core has not been identified in the catalytic cycle of known dinuclear non-heme metalloproteins, it represents an important new structural motif in the coordination chemistry of high valent non-heme diiron compounds. Its structural and electronic properties have been investigated in some detail, and the following most salient features have been established by a variety of spectroscopic and theoretical techniques:

(1) Complexes **1**−**4** containing a (μ-oxo)bis(μ-acetato)diferric core can be chemically or electrochemically one-electron oxidized yielding green compounds with an {Fe^IV(μ-O)(μ-CH₃-CO₂)₂Fe^III}^{3+} core and two identical or dissimilar tridentate nitrogen donor ligands. The valences are localized (class II).

(2) The Fe^III−O−Fe^III unit is asymmetric containing a short Fe^IV−O_b bond at 1.725 Å and a longer Fe^III−O_b bond at 1.934 Å.

(3) $\mathbf{2^{ox}}$, $\mathbf{3^{ox}}$, $\mathbf{4^{ox}}$, and $\mathbf{5^{ox}}$ each contain a single Fe(IV) ion ($S_{Fe} = 1$) with significantly shorter Fe−N_{amine} and Fe^IV−O_{carboxylato} bond distances than in the corresponding reduced species with high spin ferric ions.

(4) Extensive DFT calculations for **4**, $\mathbf{4^{ox}}$, **5** and $\mathbf{5^{ox}}$ are presented. The computational predictions of structures, EPR

(50) McGarvey, B. R. *Trans. Met. Chem.* **1966**, *3*, 89.

spectra, magnetic data, and Mössbauer spectra are in good accord with the experimental observations. We therefore conclude that the oxidized species, the structures of which presently cannot be obtained by X-ray crystallography, are very likely to indeed have the presumed identity and that the computed electronic and geometric structures for these species are realistic.

Supporting Information Available: Figures S1 and S2 displaying the magnetic susceptibilities of **4** and **1**, respectively, as a function of the temperature; Figure S3 displaying the Fourier transform of the EXAFS data for **2** and **2**[ox] and Figure S4 those for **5** and **5**[ox]. X-ray crystallographic files, in CIF format, for compound **4**. This material is available free of charge via the Internet at http://pubs.acs.org.

JA030377F